

# A mechanism for the amplification of interface distortions on liquid jets

Hanul Hwang<sup>1,†</sup>, Parviz Moin<sup>1</sup> and M.J. Philipp Hack<sup>1</sup>

<sup>1</sup>Center for Turbulence Research, Stanford University, Stanford, CA 94305, USA

(Received 22 July 2020; revised 16 October 2020; accepted 26 November 2020)

A novel mechanism for the amplification of distortions to the material interface of liquid jets is identified. The mechanism is independent of the exponential instability of the flow and can intensify small perturbations to the material interface by several orders of magnitude. Depending on the parameters, it can amplify interfacial distortions at a faster pace than modal mechanisms such as the Kelvin–Helmholtz instability. The study is based on spatial linear stability theory in a two-fluid formulation that accounts for the effects of both viscosity and surface tension. The analysis of the mechanism is cast into an optimization problem in the surface tension energy of the interface distortion and discounts the trivial redistribution of perturbation kinetic energy. The identified mechanism is related to the Orr mechanism, and amplifies distortions to the material interface via a reorientation of perturbations by the mean shear. Analyses of the linearized energy budgets show that energy is extracted from the mean shear by the production term of the streamwise perturbation velocity component and subsequently transferred to the radial perturbation velocity component, where it is absorbed by the surface tension potential of the interface. The gain in surface tension energy attributable to the mechanism is shown to scale linearly with the Reynolds number. A critical Weber number is identified as a lower bound beyond which the mechanism becomes active, and a power-law relation to the Reynolds number is established. Nonlinear simulations based on the full two-fluid Navier–Stokes equations substantiate the observability and realizability of the mechanism.

**Key words:** jets

## 1. Introduction

The atomization of liquid jets is of relevance in applications ranging from energy technology to medicine. The atomization process often begins with the amplification of small distortions to the material interface. In many settings, the growth of interface distortions is promoted by exponential instabilities that are related to the effects of surface

<sup>†</sup> Email address for correspondence: [hanul@stanford.edu](mailto:hanul@stanford.edu)

tension or the mean shear. By means of an optimization approach, this work demonstrates a new mechanism for the amplification of interface distortions on liquid jets.

Several possible pathways for the primary atomization of liquid jets exist, and their respective prevalence depends on a variety of factors, including the relative importance of surface tension and viscous forces. Stability analyses of two-liquid Poiseuille flow by Preziosi, Chen & Joseph (1989) and Lin & Ibrahim (1990) identified a linearly stable regime within a range of Reynolds numbers, which at its lower end is limited by the emergence of a capillary Plateau–Rayleigh instability. On the other hand, at sufficiently high Reynolds numbers, the shear between the two phases triggers a Kelvin–Helmholtz (K–H) instability. The K–H mode also plays an important role in the model set forth by Marmottant & Villermaux (2004) which ascribes the primary atomization of liquid jets to a series of exponential instabilities. Past the exit of the nozzle, the velocity difference between the liquid and the surrounding gas promotes a K–H instability that induces a primary distortion of the liquid interface. Depending on the flow parameters, this distortion can be either axisymmetric or helical (see e.g. Hoyt & Taylor 1977; Chigier & Eroglu 1989). Together with the difference in density between the gas and liquid phases, the primary distortion can make the flow susceptible to secondary Rayleigh–Taylor instabilities. The Rayleigh–Taylor instability gives rise to ligaments that are distributed around the circumference of the jet. Surface tension eventually induces the breakup of the ligaments by way of a Plateau–Rayleigh instability into an array of small droplets.

In addition to these inviscid instability mechanisms that rely on either surface tension or the shear between the phases, viscosity can introduce additional mechanisms for the amplification of disturbances in the two-fluid setting. Specifically, a mismatch of the viscosity in the two phases can generate viscous interfacial instabilities, as discussed by Yih (1967) and Hinch (1984). Viscosity can also give rise to instability modes that live within the shear of either phase, largely unaffected by the interface, and which are related to the Tollmien–Schlichting waves observed in single-fluid boundary layers (Yecko, Zaleski & Fullana 2002).

The identification of the specific mechanisms that promote the distortion and eventual breakup of two-fluid interfaces has often relied on linear stability theory. The classical setting considers the governing equations of small perturbations to a given base flow, which allows the disregard of nonlinear terms. The eigenvalue spectrum of the resulting linear operator identifies exponentially unstable solutions, and the associated eigenfunctions give insight into the spatial structure of the associated instability mechanism. Applications of linear theory in the two-fluid setting include the study of an air-blasted breaking liquid sheet by Lozano *et al.* (2001). They compared the results with experimental measurements of the wavenumber and amplification rate of the perturbations. Although their two-dimensional analysis quantitatively disagreed with the measurements, the consideration of viscosity in the linear analysis was deemed critical to obtain qualitative agreement. Yecko *et al.* (2002) applied linear stability theory to planar two-fluid mixing layers and investigated the influence of parameters such as the surface tension and viscosity. In the same setting, Bague *et al.* (2010) and Fuster *et al.* (2013) compared the eigensolutions computed in linear stability analyses with experimental measurements and nonlinear simulations.

Exponential growth, or modal instability, nevertheless describes only one possible path for the amplification of disturbances. Even when the eigenvalue spectrum reveals the flow as exponentially stable, disturbances can amplify through non-modal, or algebraic, mechanisms (Gustavsson 1991; Trefethen *et al.* 1993). The analysis of these types of non-exponentially growing solutions is commonly facilitated by solving an optimization problem in terms of a suitable measure, such as the perturbation kinetic energy (Reddy

### A mechanism for the amplification of interface distortions

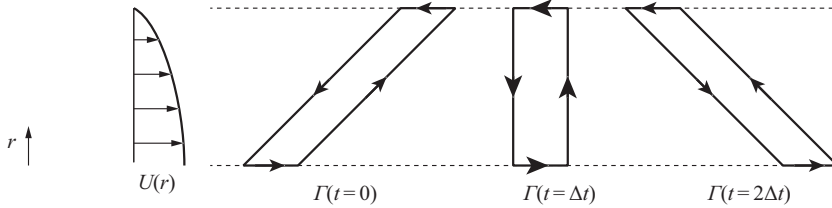


Figure 1. Illustration of the Orr mechanism. The reorientation of the initially tilted structure by the non-uniform mean flow  $U(r)$  reduces the length of the closed contour. The conservation of the circulation  $\Gamma$  thus requires a strengthening of the associated velocity.

& Henningson 1993). It has been shown that the solutions computed in the analysis of optimal disturbances qualitatively reproduce the ensemble average of perturbations sampled in flows excited by broad-band excitation (e.g. Hack & Zaki 2015). The underlying rationale is that while it is improbable to exactly observe the optimal initial condition in a realistic flow field at any given time, the projection of a random perturbation field onto this particular solution is typically non-zero and thus gives rise to energy growth.

Non-modal amplification of the perturbation in single-fluid flows such as boundary layers is most often attributable to the lift-up mechanism which describes the displacement of the mean momentum (Landahl 1975, 1980). In this setting, vortices described by the transverse and normal velocity components give rise to velocity perturbations in the streamwise velocity component, generally referred to as streaks. The coupling is nonetheless one-sided, and the streaks do not reinforce the normal and transverse fluctuations which eventually undergo viscous decay. The lift-up mechanism is most effective for perturbations at zero wavenumber in the streamwise dimension (Butler & Farrell 1992). A second pathway for the amplification of disturbances in the absence of exponential instability is provided by the Orr mechanism (Orr 1907), which intensifies perturbations by a tilting in the direction of the mean flow (see also Farrell 1987). The underlying principle is the conservation of the circulation along a closed line, as outlined in Kelvin's theorem and visualized in figure 1. In contrast to lift-up, the Orr mechanism also amplifies perturbations normal to the mean flow and is most effective for perturbations at finite streamwise wavenumber. In non-parallel flows, the two mechanisms may also occur simultaneously and lead to enhanced perturbation growth (Hack & Moin 2017).

Several studies have investigated the potential of non-modal amplification in two-fluid settings (van Noorden *et al.* 1998; Malik & Hooper 2007). Following the classical transient growth analyses in single-fluid flows, these studies considered objective functionals that were effectively posed in terms of the perturbation kinetic energy of the disturbances. In this setting, the most highly amplified perturbations were found at zero streamwise wavenumber (Yecko & Zaleski 2005) and effectively describe streamwise elongated streaks generated by the lift-up mechanism. Lift-up was also determined by Boronin, Healey & Sazhin (2013) to be the mechanism driving the transient amplification of perturbations in round liquid jets. As noted above, lift-up describes a one-sided coupling of the velocity components, with the fluctuations in the component normal to the mean shear, and thus also normal to the interface in two-fluid settings such as jets, monotonically decaying. At leading order, the liquid–gas interface is, however, kinematically coupled to the normal, but not the streamwise, fluctuation component. Perturbations amplified by lift-up, although highly intense in terms of their kinetic energy, are therefore largely irrelevant in the context of interface distortions, and by extension the advancement of the flow towards atomization. The second candidate for non-exponential amplification

of disturbances, the Orr mechanism, simultaneously amplifies both the streamwise and normal fluctuation components as visualized in [figure 1](#). As such, it has the potential to amplify distortions of the interface which may eventually trigger secondary instabilities and drive the flow towards atomization. The generally lower effectiveness of the Orr mechanism at amplifying the kinetic energy of perturbations nonetheless means that its identification requires an objective functional that focuses on the energy gain in the material interface. Moreover, Cruz-Mazo *et al.* (2017) reported the breakup of capillary jets even in the case when all the global linear modes are stable, although no direct connection to the transient amplification of disturbances was made.

In the present study, we explore a non-exponential pathway for the amplification of interface distortions of round liquid jets. The analysis is based on the solution of an optimization problem in terms of the surface tension energy. The paper is structured as follows. Section 2 presents an overview of the methodology, including a description of the linear framework and the optimization method used herein. The mechanism for the amplification of interface distortions in the absence of exponential instability is demonstrated in § 3. Analyses of the energy budget in § 4 provide further insight into the underlying physics, followed by a study into the effect of various parameters in § 5. A realization of the mechanism in a nonlinear two-fluid simulation is presented in § 6.

## 2. Methodology

In the following, we describe a conceptual framework for the analysis of linearly amplifying distortions in a liquid jet injected into a quiescent gas medium. The formulation is based on spatial stability analysis and accounts for the effects of viscosity as well as surface tension under the assumption of an axisymmetric laminar base state.

### 2.1. Base flow

The analyses employed in this work consider a linearization of the governing equations around a two-fluid base flow describing a liquid jet injected into quiescent gas. In general, the velocity distribution of axisymmetric liquid jets is governed by the distance to the nozzle exit, with the flow in the vicinity of the nozzle being influenced by the profile attained at the orifice. In an idealized configuration of a pipe with circular cross-section and constant radius connecting the nozzle to a reservoir, the product of the pipe radius  $a$  and the Reynolds number introduces a characteristic length,  $L_c = a Re$ . If the ratio of the characteristic length to the length of the pipe is large, the profile at the nozzle exit is effectively uniform, leading to an intense shear layer at the gas–liquid interface past the nozzle exit. On the other hand, for long pipes with a comparatively small characteristic length, the flow at the nozzle exit effectively describes a Hagen–Poiseuille profile (Duda & Vrentas 1967). Past the nozzle, the liquid begins to relax towards a uniform velocity distribution (González-Mendizabal, Olivera-Fuentes & Guzmán 1987; Shkadov & Sisoiev 1996), with the region of influence of the upstream flow again scaling with the product of nozzle diameter and Reynolds number. For the case of a planar jet, Söderberg & Alfredsson (1998) predict a relaxation length of  $0.36a Re$ . The relaxation process leads to comparatively intense streamwise gradients in the vicinity of the nozzle exit,  $x \lesssim 0.01a Re$  (Boronin *et al.* 2013). Downstream of this region, the streamwise gradient becomes increasingly negligible relative to the radial gradient. The linear analyses in this work thus consider a parallel base flow that is a function of the radial coordinate only, and describe a steady, laminar and axisymmetric liquid jet taken from an analytical solution, previously introduced as profile  $U_3$  in Boronin *et al.* (2013). The profile is representative of a nozzle

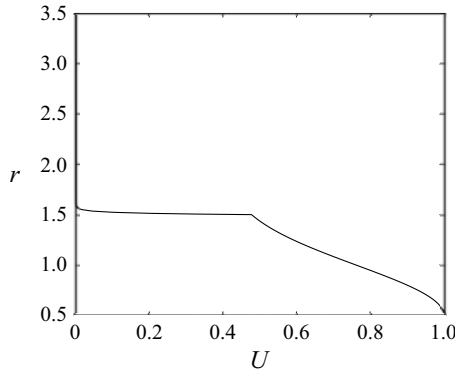


Figure 2. Base flow of liquid jet in stationary gas. The material interface is located at  $r = 1$ .

that is sufficiently long to allow the development of the flow into a Hagen–Poiseuille profile.

Throughout this work,  $x$ ,  $r$  and  $\theta$  denote the axial, radial and azimuthal directions, respectively, and  $u$ ,  $v$  and  $w$  denote the velocity disturbances in these dimensions. All quantities are normalized by the the radius of the liquid jet,  $R$ , and its centreline velocity,  $U_c$ . We further introduce a decomposition of the velocity vector  $\mathbf{u} = (u, v, w)^T$  into a mean, or base flow and a small perturbation component:

$$\mathbf{u}(x, r, \theta, t) = \bar{\mathbf{u}}(r) + \mathbf{u}'(x, r, \theta, t). \tag{2.1}$$

The analytical expressions for the base flow velocity profiles in the liquid and gas phases, respectively, are

$$\left. \begin{aligned} \bar{u}_l(r) &= \alpha_l \exp\left(\frac{-r^2}{\delta_l^2}\right) + \beta_l, & 0 < r < 1, \\ \bar{u}_g(r) &= \alpha_g \exp\left\{\frac{-(r-r_g)^2}{\delta_g^2}\right\}, & r > 1. \end{aligned} \right\} \tag{2.2}$$

Here and throughout the paper, the indices  $g$  and  $l$  denote quantities taken from the gas and liquid phases, respectively. Following Boronin *et al.* (2013), we choose  $\alpha_l = 0.6$ ,  $\beta_l = 0.4$ ,  $r_l = 0$ ,  $\delta_l = 0.7$  and  $\delta_g = 0.25$ . The parameters  $\alpha_g$  and  $r_g$  are determined so as to satisfy the interfacial continuity of velocity and stress in the streamwise velocity component. We note that the streamwise expansion of the jet balances the radial diffusion. However, the resulting streamwise gradients are small and are thus disregarded. A visualization of the streamwise invariant base flow profile is presented in figure 2.

The radial extent of the computational domain is three jet radii,  $L_r = 3$ .

We further introduce a set of non-dimensional parameters, including the Reynolds number

$$Re = \frac{\rho_l U_c R}{\mu_l}, \tag{2.3}$$

with  $\rho_l$  the fluid density. The Weber number is defined as

$$We = \frac{\rho_l U_c^2 R}{\sigma}, \tag{2.4}$$

with  $\sigma$  denoting the interfacial surface tension. The set of non-dimensional parameters describing the two-fluid problem is completed by the ratio of the densities of the two media,

$$\eta = \frac{\rho_g}{\rho_l}, \tag{2.5}$$

and the ratio of their viscosities,

$$m = \frac{\mu_g}{\mu_l}. \tag{2.6}$$

### 2.2. Linear stability equations

We consider the dynamics of small disturbances to the jet, as described by the linearized Navier–Stokes equations in cylindrical coordinates:

$$\frac{\partial u'}{\partial t} + \bar{u} \frac{\partial u'}{\partial x} + v' \frac{\partial \bar{u}}{\partial r} = -\frac{\partial p'}{\partial x} + \frac{1}{Re} \nabla^2 u', \tag{2.7}$$

$$\frac{\partial v'}{\partial t} + \bar{u} \frac{\partial v'}{\partial x} = -\frac{\partial p'}{\partial r} + \frac{1}{Re} \left( \nabla^2 v' - \frac{v'}{r^2} - \frac{2}{r^2} \frac{\partial w'}{\partial \theta} \right), \tag{2.8}$$

$$\frac{\partial w'}{\partial t} + \bar{u} \frac{\partial w'}{\partial x} = -\frac{1}{r} \frac{\partial p'}{\partial \theta} + \frac{1}{Re} \left( \nabla^2 w' + \frac{2}{r^2} \frac{\partial v'}{\partial \theta} - \frac{w'}{r^2} \right), \tag{2.9}$$

$$\frac{\partial u'}{\partial x} + \frac{1}{r} \frac{\partial}{\partial r}(rv') + \frac{1}{r} \frac{\partial w'}{\partial \theta} = 0, \tag{2.10}$$

with the Laplace operator in cylindrical coordinates defined as  $\nabla^2 = (\partial^2/\partial x^2) + (1/r)(\partial/\partial r)(r(\partial/\partial r)) + (1/r^2)(\partial^2/\partial \theta^2)$ . We note that in contrast to formulations in terms of the radial velocity and vorticity, as proposed for instance in Schmid & Henningson (1994), the present formulation, (2.7)–(2.10), is limited to spatial derivatives of second order.

The streamwise-invariant, axisymmetric and steady base flow introduced in § 2.1 allows a normal-mode ansatz for the disturbances, which are assumed to be of the form

$$[u', v', w', p'] = [\hat{u}(r), \hat{v}(r), \hat{w}(r), \hat{p}(r)] \exp(i(\alpha x + n\theta - \omega t)). \tag{2.11}$$

In the same manner, the disturbance of the interface between the two phases  $f'$  is expressed as

$$f' = \hat{f} \exp(i(\alpha x + n\theta - \omega t)). \tag{2.12}$$

Here,  $\alpha$  and  $n$  denote the streamwise and discrete azimuthal wavenumbers, respectively, and  $\omega$  represents the frequency of the disturbance. The spatial discretization in the inhomogeneous radial dimension is based on two sets of Chebyshev polynomials that represent the flow in the two phases. The liquid phase uses  $N_l = 120$  Chebyshev collocation points, and  $N_g = 70$  collocation points are employed in the gas phase.

Substitution of the ansatz (2.11) into the governing equations (2.7)–(2.10) leads to

$$\left\{ -\frac{1}{Re} \frac{\partial^2}{\partial r^2} - \frac{1}{Re} \frac{1}{r} \frac{\partial}{\partial r} + \left[ -i\omega + i\alpha\bar{u} + \frac{1}{Re} \left( \frac{n^2}{r^2} + \alpha^2 \right) \right] \right\} \hat{u} + i \frac{\partial \bar{u}}{\partial r} \hat{v} + i\alpha \hat{p} = 0, \quad (2.13)$$

$$\left\{ -\frac{1}{Re} \frac{\partial^2}{\partial r^2} - \frac{1}{Re} \frac{1}{r} \frac{\partial}{\partial r} + \left[ -i\omega + i\alpha\bar{u} + \frac{1}{Re} \left( \frac{n^2 + 1}{r^2} + \alpha^2 \right) \right] \right\} \hat{v} + \frac{i}{Re} \frac{2n}{r^2} \hat{w} + \frac{\partial}{\partial r} \hat{p} = 0, \quad (2.14)$$

$$\left\{ -\frac{1}{Re} \frac{\partial^2}{\partial r^2} - \frac{1}{Re} \frac{1}{r} \frac{\partial}{\partial r} + \left[ -i\omega + i\alpha\bar{u} + \frac{1}{Re} \left( \frac{n^2 + 1}{r^2} + \alpha^2 \right) \right] \right\} \hat{w} - \frac{1}{Re} \frac{2n}{r^2} \hat{v} + i \frac{n}{r} \hat{p} = 0, \quad (2.15)$$

$$i\alpha \hat{u} + \frac{1}{r} \frac{\partial}{\partial r} \hat{v} + i \frac{n}{r} \hat{w} = 0. \quad (2.16)$$

The interface disturbance is assumed to be small and is related to the radial disturbance velocity component through the kinematic condition

$$\frac{Df'}{Dt} = \left( -i\omega + i\alpha\bar{u}_I' \right) \hat{f} \exp(i(\alpha x + n\theta - \omega t)) = \hat{v}_I' \exp(i(\alpha x + n\theta - \omega t)), \quad (2.17)$$

where  $(D/Dt) = (\partial/\partial t) + (\bar{u}(\partial/\partial x))$  denotes the material derivative and the superscript  $I$  denotes quantities evaluated at the interface.

### 2.3. Boundary and interface conditions

The solution of the governing equations (2.13)–(2.16) requires the prescription of boundary and interface conditions. At the outer boundary of the computational domain, in the far field of the gas phase, no-slip and no-penetration boundary conditions are imposed on the eigenfunctions:

$$\hat{u}_g = 0, \quad \hat{v}_g = 0, \quad \hat{w}_g = 0 \quad \text{at } r = L_r. \quad (2.18)$$

Special care has to be taken at the centreline because of the singular nature of the cylindrical coordinate system. The assumption of smooth and bounded behaviour of all physical quantities at the centreline,  $r \rightarrow 0$ , implies that (see e.g. Khorrami, Malik & Ash 1989)

$$\lim_{r \rightarrow 0} \frac{\partial \hat{\mathbf{u}}}{\partial \theta} = \frac{\partial}{\partial \theta} (\hat{u} \mathbf{e}_z + \hat{v} \mathbf{e}_r + \hat{w} \mathbf{e}_\theta) = 0, \quad (2.19)$$

and for the pressure

$$\lim_{r \rightarrow 0} \frac{\partial \hat{p}}{\partial \theta} = 0. \quad (2.20)$$

Substitution of the normal-mode ansatz (2.11) into (2.19)–(2.20) yields

$$n\hat{v} + \hat{w} = 0, \quad (2.21)$$

$$\hat{v} + n\hat{w} = 0, \quad (2.22)$$

$$n\hat{u} = 0, \quad (2.23)$$

$$n\hat{p} = 0. \quad (2.24)$$

The resulting centreline conditions depend on the discrete azimuthal number,  $n$ , as follows:

$$\frac{\partial \hat{u}}{\partial r} = 0, \quad \hat{v} = 0, \quad \hat{w} = 0, \quad \frac{\partial \hat{p}}{\partial r} = 0 \quad \text{for } n = 0, \tag{2.25}$$

$$\hat{u} = 0, \quad -i\hat{v} + n\hat{w} = 0, \quad -2i\frac{\partial \hat{v}}{\partial r} + n\frac{\partial \hat{w}}{\partial r} = 0, \quad \hat{p} = 0 \quad \text{for } n = -1 \text{ or } 1, \tag{2.26}$$

$$\hat{u} = 0, \quad \hat{v} = 0, \quad \hat{w} = 0, \quad \hat{p} = 0 \quad \text{otherwise.} \tag{2.27}$$

We note that because of the linear dependence of conditions (2.21) and (2.22) in the case  $|n| = 1$ , one of the conditions for that case was derived by applying the continuity equation (2.16).

At the interface ( $r = 1$ ), both the velocity and stress are continuous in the radial dimension. In the parallel velocities and tangential stresses, the differences across the interface are proportional to the surface tension and mean gradient, respectively:

$$\mathcal{J}(\hat{u}) = \mathcal{J}\left(\frac{\partial \bar{u}}{\partial r}\right)\hat{f}, \quad \mathcal{J}(\hat{v}) = 0, \quad \mathcal{J}(\hat{w}) = 0, \tag{2.28a-c}$$

$$\mathcal{J}(\hat{\tau}_{zr}) = \mathcal{J}\left(\mu\frac{\partial^2 \bar{u}}{\partial r^2}\right)\hat{f}, \quad \mathcal{J}(\hat{\tau}_{\theta r}) = 0, \quad \mathcal{J}(\hat{\tau}_{rr}) = \sigma\nabla^2\hat{f}. \tag{2.29a-c}$$

Here,  $\mathcal{J}(\mathcal{X})$  denotes the difference in  $\mathcal{X}$  between the two phases at the interface. We note that the relations for  $\hat{u}$  and  $\hat{\tau}_{zr}$  have been derived by employing first-order Taylor expansions, implying that  $\bar{u}_j(r = 1 + f) = \bar{u}_j^l + (d\bar{u}_j^l/dr)\hat{f}$ . The resulting interface conditions are

$$\mathcal{J}\left(i\mu\alpha\hat{v} + \mu\frac{\partial \hat{u}}{\partial r}\right) = \mathcal{J}\left(\mu\frac{\partial^2 \bar{u}}{\partial r^2}\right)\hat{f}, \tag{2.30a}$$

$$\mathcal{J}\left(\mu\left(\frac{\partial}{\partial r} - 1\right)\hat{w} + i\mu n\hat{v}\right) = 0, \tag{2.30b}$$

$$\mathcal{J}\left(-\frac{\rho}{\rho_1}\hat{p} + \frac{2}{Re}\frac{\mu}{\mu_1}\frac{\partial \hat{v}}{\partial r}\right) = -\frac{1}{We}\left(1 - n^2 - \alpha^2\right)\hat{f}. \tag{2.30c}$$

#### 2.4. Spatial linear analysis

The linearized equations (2.13)–(2.16) permit solutions of both temporally and spatially developing solutions. In this work, we focus exclusively on the spatial case which more faithfully represents the amplification of perturbations in the shear layer of the liquid jet. Spatial stability analysis prescribes a real-valued frequency  $\omega$  and azimuthal wavenumber  $n$  of the disturbances. As a consequence, only certain complex wavenumbers  $\alpha$  satisfy the stability equations (2.13)–(2.16), which gives rise to an eigenvalue problem of the form

$$i\alpha\mathbf{M}\hat{\mathbf{q}} = \mathbf{L}\hat{\mathbf{q}}. \tag{2.31}$$

Here,  $\hat{\mathbf{q}}$  is the disturbance state vector

$$\hat{\mathbf{q}} = \left[\hat{\phi}_g(r) \hat{f} \quad \alpha\hat{f} \quad \hat{\phi}_l(r)\right]^T, \tag{2.32}$$



with

$$\hat{\phi}_i = [\hat{u}_i(r) \ \hat{v}_i(r) \ \hat{w}_i(r) \ \hat{p}_i(r) \ \alpha \hat{u}_i(r) \ \alpha \hat{v}_i(r) \ \alpha \hat{w}_i(r)]^T. \quad (2.33)$$

The operators  $\mathbf{M}$  and  $\mathbf{L}$  are given in [appendix A](#).

Since our focus is on the study of disturbances in the absence of exponential instability, we restrict our analyses to exponentially stable settings in which all eigensolutions of the spatial stability problem (2.31) decay in  $x$ . While the sign of the eigenvalue reveals the stability of the eigensolution in temporal analysis, the nonlinear spatial eigenvalue problem prevents such immediate classification. Existing approaches to the identification of the stability properties of spatial modes involve iterative schemes as applied for instance by Lin & Chen (1998) and Boronin *et al.* (2013). In the present work, we directly determine the spatial stability of individual eigenfunctions by evaluating their group velocity,

$$c_g \equiv \frac{\partial \omega}{\partial \alpha}, \quad (2.34)$$

using information provided by the adjoint stability equations. More specifically, a positive spatial growth rate, i.e. a negative imaginary part of  $\alpha$ , implies spatial growth if the mode travels downstream, indicated by a positive group velocity. If the group velocity of the eigenfunction is negative, it travels upstream and thus undergoes decay. Analogously, a mode with a negative spatial growth rate, i.e. a positive imaginary part of  $\alpha$ , will decay if its group velocity is positive, and amplify if its group velocity is negative.

In this context, we define the inner product as the volume integrated dot product within the computational domain:

$$\langle \mathbf{a}, \mathbf{b} \rangle = \int_{\Omega} \mathbf{a}^H \mathbf{b} \, dV, \quad (2.35)$$

with superscript  $H$  denoting the complex conjugate transpose. The adjoint eigenfunctions,  $\hat{\mathbf{q}}^\dagger$ , are the solution of the adjoint eigenvalue problem

$$\alpha^* \mathbf{M}^H \hat{\mathbf{q}}^\dagger = \mathbf{L}^H \hat{\mathbf{q}}^\dagger, \quad (2.36)$$

where superscript  $*$  denotes complex conjugate. Solutions to the forward and adjoint eigenvalue problem satisfy a bi-orthogonality condition, so that upon proper normalization

$$\langle \hat{\mathbf{q}}_i^\dagger, \mathbf{M} \hat{\mathbf{q}}_j \rangle = \delta_{ij}. \quad (2.37)$$

We derive a relation for the group velocity by applying the partial derivative with respect to  $\omega$  to (2.31), and integrating over the computational domain:

$$\frac{\partial \alpha}{\partial \omega} \langle \hat{\mathbf{q}}^\dagger, \mathbf{M} \hat{\mathbf{q}} \rangle = \left\langle \hat{\mathbf{q}}^\dagger, \frac{\partial \mathbf{L}}{\partial \omega} \hat{\mathbf{q}} \right\rangle. \quad (2.38)$$

Application of the bi-orthogonality condition (2.37) to (2.38) leads to

$$\frac{\partial \alpha}{\partial \omega} = \left\langle \hat{\mathbf{q}}^\dagger, \frac{\partial \mathbf{L}}{\partial \omega} \hat{\mathbf{q}} \right\rangle. \quad (2.39)$$

The group velocity of an eigenfunction  $\hat{\mathbf{q}}$ , and by extension its exponential stability within the spatial stability framework, may thus be evaluated by the inner product with its corresponding adjoint eigenvector  $\hat{\mathbf{q}}^\dagger$ :

$$\frac{\partial \omega}{\partial \alpha} = \left\langle \hat{\mathbf{q}}^\dagger, \frac{\partial \mathbf{L}}{\partial \omega} \hat{\mathbf{q}} \right\rangle^{-1}. \quad (2.40)$$

We note that while iterative approaches require multiple solutions of the stability problem for each individual mode, the gradient information provided by the adjoint problem

identifies the group velocity of all eigensolutions after solving the adjoint eigenvalue problem (2.36) once.

### 2.5. Optimization problem

Even when all the eigensolutions of the spatial stability problem (2.31) are stable, the non-normal nature of the linearized Navier–Stokes equations provides a pathway for disturbance growth. The study of this non-modal, or transient, amplification of disturbances can be facilitated by considering an optimization problem in a suitably chosen norm. Earlier analyses of non-modal growth in the two-fluid setting followed studies in single-fluid shear flows in effectively optimizing the kinetic energy of disturbances (e.g. Renardy 1987; Yecko & Zaleski 2005; Boronin *et al.* 2013). In the wider context of flow atomization, the amplification of distortions specifically of the material interface is nonetheless of greater relevance.

We investigate the specific conditions that amplify distortions of the interface by introducing an interface energy norm of the form

$$\|q\|_{IE} = \int_0^{2\pi/n} \int_0^{2\pi/\omega} \frac{1}{We} (-1 + n^2 + \alpha^2) \hat{f}^* \hat{f} \, dt \, d\theta. \tag{2.41}$$

The norm represents a measure for the surface tension energy stored in the material interface owing to the perturbation displacement  $\hat{f}$ . The derivation is presented in appendix B. Together with the norm (2.41), we introduce the suitably chosen weight matrix  $\mathbf{F}$  which allows the transformation of the interface energy norm into a 2-norm so that  $\|q\|_{IE} \equiv \|\mathbf{F}q\|_2$ . We note that the interface energy norm (2.41) partitions the state vector and as such describes a non-trivial semi-norm. As a consequence,  $\mathbf{F}$  is rank-deficient. Specifically, the velocity and pressure components of both the gas and liquid phases are within the kernel of  $\mathbf{F}$ . The formulation of a well-posed optimization problem thus calls for the introduction of a full norm (see e.g. Foures, Caulfield & Schmid 2012), which we choose as the total energy norm:

$$\begin{aligned} \|q\|_E &= \frac{1}{2} \eta \int_1^{L_r} \int_0^{2\pi/n} \int_0^{2\pi/\omega} \left( \hat{u}_g^* \hat{u}_g + \hat{v}_g^* \hat{v}_g + \hat{w}_g^* \hat{w}_g \right) r \, dt \, d\theta \, dr \\ &\quad + \frac{1}{2} \int_0^1 \int_0^{2\pi/n} \int_0^{2\pi/\omega} \left( \hat{u}_l^* \hat{u}_l + \hat{v}_l^* \hat{v}_l + \hat{w}_l^* \hat{w}_l \right) r \, dt \, d\theta \, dr \\ &\quad + \int_0^{2\pi/n} \int_0^{2\pi/\omega} \frac{1}{We} (-1 + n^2 + \alpha^2) \hat{f}^* \hat{f} \, dt \, d\theta. \end{aligned} \tag{2.42}$$

Analogous to the interface energy norm, the energy norm can be converted to a 2-norm by means of the matrix  $\mathbf{F}_N$ , with  $\|q\|_E \equiv \|\mathbf{F}_N q\|_2$ . Since (2.42) covers all components of the state vector, the null space of  $\mathbf{F}_N$  is empty.

Our optimization problem seeks to find the specific, optimal, initial condition  $q_0$ , which over a prescribed spatial distance evolves into the particular final condition  $q_1$  that induces the most energetic distortions of the jet interface, as measured by the norm  $\|q\|_{IE}$ . In our solution of the optimization problem, we follow Hack & Moin (2017) in expressing the initial condition as a weighted sum of eigenfunctions of the two-fluid stability problem (2.31):

$$q_0 = \mathbf{Q}_0 \kappa. \tag{2.43}$$

Here, the columns of  $\mathbf{Q}_0 \in \mathbb{C}^{N_Q \times N}$ , where  $N_Q = 7N_l + 7N_g + 2$ , contain the  $N$  least stable eigenfunctions  $\hat{q}_{j,0}$  and  $\kappa \in \mathbb{C}^{N \times 1}$  assigns each of the modes a specific weight.

Consistently, the solution at the final position  $x_1$  may be expressed as

$$\mathbf{q}_1 = \mathbf{Q}_1 \boldsymbol{\kappa}, \quad (2.44)$$

with the columns of  $\mathbf{Q}_1$  representing the evolution of the  $n$  eigenfunctions:

$$\hat{q}_{j,1} = \hat{q}_{j,0} \exp(i\alpha_j(x_1 - x_0)). \quad (2.45)$$

The linear nature of the problem implies that  $\boldsymbol{\kappa}$  is identical in both expressions. Since  $\mathbf{Q}_0$  has full column rank, we can explicitly determine its Moore–Penrose pseudo-inverse  $\mathbf{Q}_0^+ = (\mathbf{Q}_0^H \mathbf{Q}_0)^{-1} \mathbf{Q}_0^H$ , leading to

$$\mathbf{Q}_0^+ \mathbf{q}_0 = \boldsymbol{\kappa}. \quad (2.46)$$

Substitution into (2.44) yields

$$\mathbf{q}_1 = \mathbf{L}_1 \mathbf{q}_0, \quad (2.47)$$

where  $\mathbf{L}_1 = \mathbf{Q}_1 \mathbf{Q}_0^+$  is a pseudo-propagator that advances arbitrary initial disturbances  $\mathbf{q}_0$  within the column space of  $\mathbf{Q}_0$  from  $x_0$  to  $x_1$ . Without loss of generality, we choose  $x_0 = 0$  in this work.

The objective of finding the specific initial condition  $\mathbf{q}_0$  that maximizes the amplification of interface distortions with frequency  $\omega$  at a given target location  $x_1$  may thus be expressed as the functional

$$G(\omega, x_1) = \frac{1}{2} \max_{\mathbf{q}_0} \frac{\|\mathbf{q}_1\|_{IE}^2}{\|\mathbf{q}_0\|_E^2} \quad (2.48)$$

$$= \frac{1}{2} \max_{\mathbf{q}_0} \frac{\|\mathbf{L}_1 \mathbf{q}_0\|_{IE}^2}{\|\mathbf{L}_0 \mathbf{q}_0\|_E^2} \quad (2.49)$$

$$= \frac{1}{2} \|\mathbf{F} \mathbf{L}_1 (\mathbf{F}_N \mathbf{L}_0)^+\|_2^2. \quad (2.50)$$

Here,  $\mathbf{q}_1 = \mathbf{q}(x_1)$  and the introduction of  $\mathbf{L}_0 = \mathbf{Q}_0 \mathbf{Q}_0^+$  into the denominator restricts  $\mathbf{q}_0$  to the column space of  $\mathbf{Q}_0$ . We further note that the majority of the results presented in the following focus on the maximum gain, which represents the maximum  $G$  for all possible perturbation frequencies and target locations,  $G_{max} = \max_{\omega, x_1} G(\omega, x_1)$ .

The objective functional  $G$  relates the interface energy at the target position  $x_1$  to the sum of the kinetic and interface perturbation energies at the initial position  $x_0$ . In other words,  $G$  quantifies the interface energy at the target location normalized by the total initial perturbation energy. In doing so, it prescribes a fair and conservative measure for the amplification of interface distortions as  $G$  attains values larger than unity only if the perturbation interface energy at the considered target location exceeds the total energy at the initial location  $x_0$ , i.e. if energy has been extracted from the mean shear and redistributed into the potential energy of the interface. A trivial redistribution of initial perturbation kinetic energy into perturbation interface energy at the target location therefore does not add to the gain. We also note that the pre-factor of  $\frac{1}{2}$  has been added for convenience only. In its absence, the critical value separating genuine amplification from decay or trivial redistribution would be 2. In what follows, we apply the conceptual framework presented above in the demonstration of the linear amplification of distortions to the interface of a liquid jet by a non-exponential mechanism.

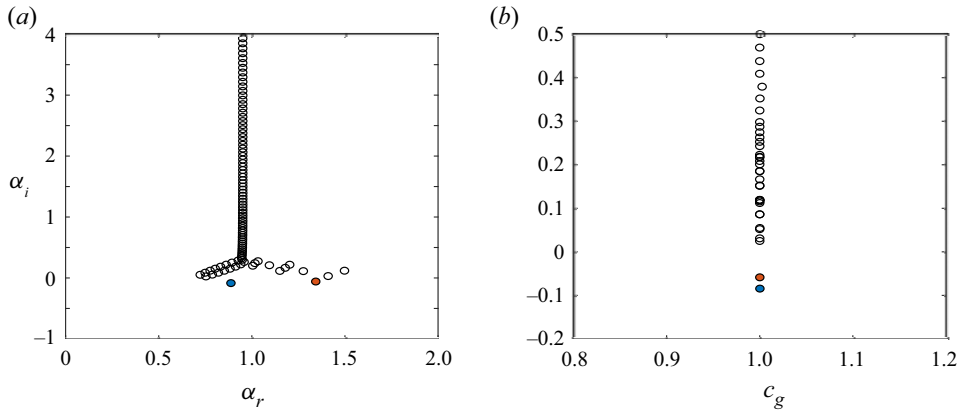


Figure 3. (a) Spectrum of the complex eigenvalue  $\alpha$  for  $Re = 7500$ ,  $We = 3000$ ,  $m = 0.01$ ,  $\eta = 0.001$ ,  $n = 1$  and  $\omega = 0.7$ . (b) Group velocity  $c_g$  and growth rate  $\alpha_i$  of the eigenfunctions. Blue and red circles mark the unstable modes.

### 3. Mechanism for the amplification of interface distortions

In the following, we demonstrate a mechanism that allows the amplification of distortions to the material interface of a liquid jet in exponentially stable settings. In a first step, we analyse the linear stability of a jet described by profile (2.2) by solving the spatial stability problem (2.31) for the considered parameters  $Re = 7500$ ,  $We = 3000$ ,  $m = 0.01$ ,  $\eta = 0.001$ ,  $n = 1$  and  $\omega = 0.7$ . We note that the considered viscosity and density ratios are comparable to those of the combination of water and air. Figure 3(a) presents the real and imaginary parts of the computed eigenvalues in terms of the complex streamwise wavenumber,  $\alpha$ , of the disturbances. The polynomial nature of the spatial stability problem impedes a classification of the exponential stability of eigensolutions based on the sign of the eigenvalue alone, as discussed in § 2.4. The determination of the stability of a given eigensolution instead has to consider both the eigenvalue and the associated group velocity. For the present setting, figure 3(b) presents the group velocities of the individual eigenvalues along with the imaginary parts of the wavenumber. The group velocity is positive for all considered eigenvalues, and the two eigensolutions with negative  $\alpha_i$  are thus exponentially unstable while all other modes with  $\alpha_i > 0$  are stable.

The imaginary parts of the eigenvalues,  $\alpha_i$ , of the respective least stable modes at eight different azimuthal numbers,  $n$ , are presented in figure 4 as a function of the disturbance frequency  $\omega$ . The parameters are  $Re = 7500$ ,  $We = 3000$ ,  $m = 0.01$  and  $\eta = 0.001$ , and the considered azimuthal wavenumbers range from  $n = 0$  to  $n = 7$ . In all cases, the corresponding group velocities are positive, and the sign of the eigenvalues thus determines the stability of the solutions. The modes computed for  $n = 0$  to  $n = 4$  are exponentially unstable for certain perturbation frequencies. The highest amplification occurs for  $n = 1$ , which is referred to as the sinuous mode of the K–H instability (Söderberg 2003). For  $n > 4$ , the most unstable modes decay for all considered frequencies. Our analyses of the transient amplification of interface perturbations thus focus on this wavenumber range. Analogous to the optimal modes with non-zero transverse wavenumber considered by Yecko & Zaleski (2005), these non-axisymmetric modes directly provide a pathway for the generation of transverse perturbations.

The solution of the optimization problem in the interface energy norm  $\|q\|_{IE}$  establishes that a significant amplification of interfacial distortions can occur in the absence of exponential instability. The 2-norm of the operator  $\mathbf{FL}_1(\mathbf{F}_N\mathbf{L}_0)^+$  is determined by the

## A mechanism for the amplification of interface distortions

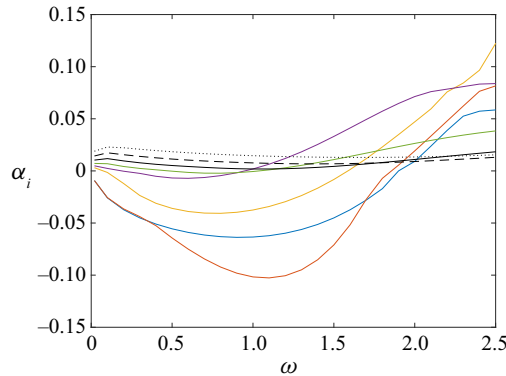


Figure 4. Spatial growth rate  $\alpha_i$  as a function of the disturbance frequency  $\omega$  for the least stable modes at azimuthal wavenumbers  $n = 0$  (blue),  $n = 1$  (red),  $n = 2$  (yellow),  $n = 3$  (purple),  $n = 4$  (green),  $n = 5$  (black solid),  $n = 6$  (black dashed) and  $n = 7$  (black dotted). The parameters are  $Re = 7500$ ,  $We = 3000$ ,  $m = 0.01$  and  $\eta = 0.001$ .

singular value decomposition:

$$\mathbf{U}\boldsymbol{\Sigma}\mathbf{V}^H = \mathbf{F}\mathbf{L}_1(\mathbf{F}_N\mathbf{L}_0)^+. \quad (3.1)$$

Here,  $\mathbf{U}$  is an orthogonal matrix whose columns are the left singular vectors, and the columns of  $\mathbf{V}$  contain the right singular values. The entries of the real, positive definite diagonal matrix  $\boldsymbol{\Sigma}$  describe the singular values  $\sigma_j$ . Specifically, the largest singular value describes the gain,  $G \equiv \sigma_{max}$ , and the associated right singular vector gives the corresponding initial state. The parameters are  $Re = 7500$ ,  $We = 3000$ ,  $m = 0.01$ ,  $\eta = 0.001$ ,  $n = 5$  and  $\omega = 2.2$  and the target location is  $x_1 = 11.8$ . The amplification of the distortion to the material interface is quantified by evaluating the magnitude of the interface displacement,  $f$ . The absolute value of the interface distortion, normalized by its initial value, is presented in figure 5(a) as a function of the streamwise coordinate. The maximum amplification ratio of the interface distortion at  $x = 11.8$  is  $|f(x)/f_0| \simeq 1042$ . The growth of the interface distortion towards the target location,  $x_1$ , shows an oscillatory, non-monotonic behaviour. The streamwise evolution of the integrated kinetic energy in the velocity perturbations and surface potential energy is presented in figure 5(b,c). The kinetic energy in all components generally increases from the initial location  $x_0$  to the target location  $x_1 = 11.8$ . While the energy in the streamwise components gains most, we note that the azimuthal and critically the radial components also amplify. In contrast to the streamwise and azimuthal components, the gain in the radial perturbations is non-monotonic, and the energy in that component is below its peak at the target location. Analogously, the trend in the interface potential energy is non-monotonic, although the peak of this quantity coincides with the target location. As we demonstrate in § 4, the non-monotonic increase in both the interface displacement and the kinetic energy in the radial velocity perturbations is related to a temporary redistribution between the potential energy in the interface due to surface tension and the kinetic energy of the velocity perturbations.

The significance of the non-exponential amplification of the interface distortion is established by comparing with the fastest-growing exponential instability, which occurs for an azimuthal wavenumber  $n = 1$  (see figure 4). The growth rate of the mode is  $\alpha_i = 0.1028$ , leading to an expected growth of the most unstable mode during the considered interval of  $\exp(\alpha_i x_1) = \exp(0.1028 \times 11.8) = 3.364$ , which is significantly smaller than

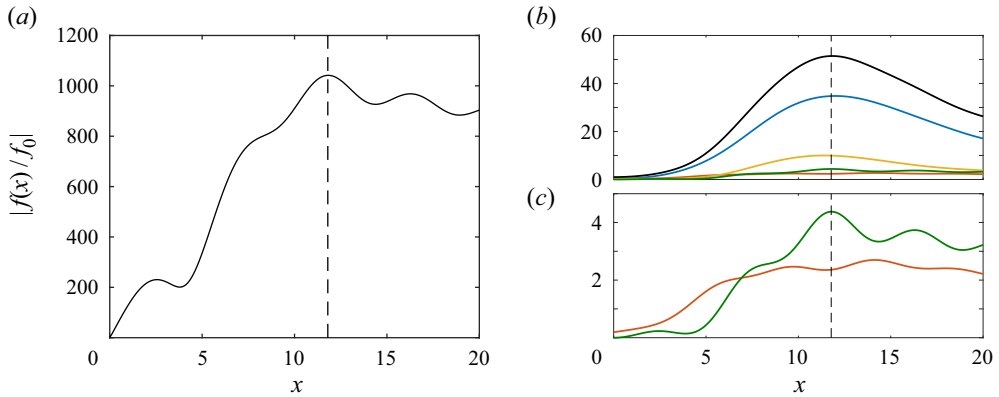


Figure 5. (a) Spatial evolution of the absolute value of the ratio of interface disturbance amplitude. (b) Spatial evolution of the integrated kinetic energy in the streamwise velocity component (blue), radial velocity component (red) and azimuthal component (yellow), their sum (black) and surface tension energy of the interface perturbation (green). (c) Detail showing the spatial evolution of the integrated kinetic energy in the radial velocity component (red) and surface tension energy of the interface perturbation (green). The dashed lines mark the target location,  $x_1 = 11.8$ . The parameters are  $Re = 7500$ ,  $We = 3000$ ,  $m = 0.01$ ,  $\eta = 0.001$ ,  $n = 5$  and  $\omega = 2.2$ .

the ratio of  $|f(x)/f_0| \simeq 1042$  reported for the optimal interface distortion. This result demonstrates that over finite streamwise intervals, the algebraic amplification of interface distortions by means of the presented mechanism may considerably exceed that by the exponential K–H instability.

A visualization of the spatial evolution of the disturbance field is presented in figure 6. Vectors mark the streamwise and radial perturbation velocities,  $u'$  and  $v'$ , in the  $x$ – $r$  plane and colour contours show the azimuthal component,  $w'$ , of the perturbation velocity. The growth in the intensity of the perturbation velocities coincides with a reorientation of the initially tilted fluid structure by the mean shear. As a consequence, the distortion of the material interface is amplified and peaks at  $x = 11.8$ , marked by the vertical dashed line. Both the tilting of the perturbation structures and the amplification of velocity perturbations normal to the direction of the mean shear are characteristic of the Orr mechanism, as sketched in figure 1. In the two-fluid setting, these perturbations are also normal to the the material interface, and thus induce an amplification of interface distortions.

We note that the presented outcome qualitatively differs from that of the lift-up mechanism which generates low-frequency perturbations in the streamwise perturbation velocity component (e.g. Gustavsson 1991; Hack & Zaki 2015) and which was identified in earlier analyses of non-exponentially amplifying disturbances in two-fluid settings (Yecko & Zaleski 2005; Boronin *et al.* 2013). Owing to the kinematic coupling of the interface distortion to the velocity component normal to the interface, these perturbations are, however, unlikely to meaningfully advance the atomization process. The present analysis of perturbations which induce a significant amplification of the distortion of the material interface by means of the Orr mechanism is facilitated by the choice of the objective functional in terms of the perturbation interface energy (2.41). This approach differs from the optimization of the total energy of the perturbations, as considered in previous studies (e.g. South & Hooper 1999; Yecko & Zaleski 2005).

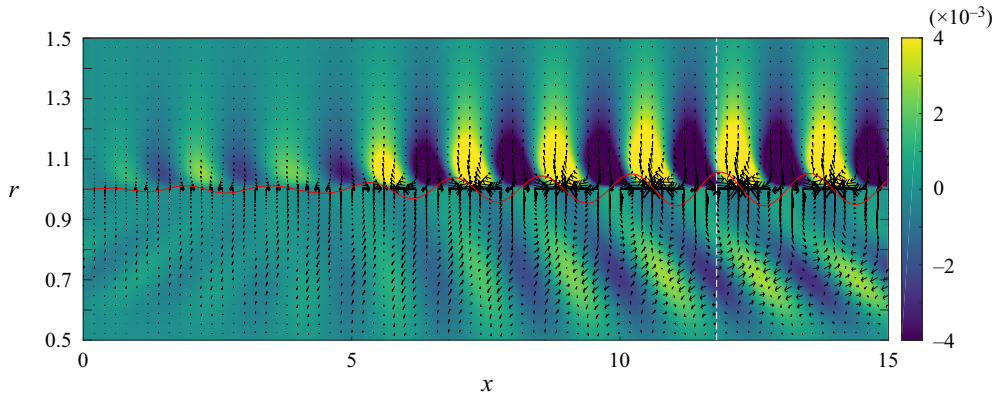


Figure 6. Side view of the streamwise evolution of the optimal initial condition. Vectors of the streamwise and radial disturbance fields,  $u'$  and  $v'$ , with colour contours of the azimuthal disturbance field,  $w'$ . The red line marks the position of material interface. The white dashed line marks the target location,  $x_1$ . The parameters are  $Re = 7500$ ,  $We = 3000$ ,  $m = 0.01$ ,  $\eta = 0.001$ ,  $n = 5$  and  $\omega = 2.2$ .

#### 4. Energy budget

In the following, we seek to provide a more comprehensive documentation of the presented mechanism for amplifying interface distortions by examining the budget of the perturbation kinetic energy. The energy budget is derived by taking the dot product of the linearized governing equations, (2.7)–(2.9), with the velocity perturbation vector for each phase and substituting the continuity equation, (2.10), as well as the interface coupling condition (2.29). Our analyses of the energy budget will focus on integral quantities, defined in terms of the spatio-temporal integral

$$\int_{\Omega} \chi \, d\Omega = \int_0^x \int_0^{2\pi/\omega} \int_0^{2\pi/n} \int_0^1 \chi r \, dr \, d\theta \, dt \, dx. \quad (4.1)$$

Similarly, spatio-temporal integration on the jet interface for a quantity of interest,  $\chi$ , is denoted as

$$\int_S \chi \, dS = \int_0^x \int_0^{2\pi/\omega} \int_0^{2\pi/n} [\chi]_{r=1} \, d\theta \, dt \, dx. \quad (4.2)$$

The linearized energy budgets for the three perturbation velocity components thus are

$$\begin{aligned} \int_{\Omega} \frac{D}{Dt} \left( \frac{1}{2} u'^2 \right) d\Omega &= \underbrace{\int_{\Omega} p' \frac{\partial u'}{\partial x} \, d\Omega}_{\text{Pressure-velocity correlation}} + \underbrace{\int_{\Omega} \frac{\partial}{\partial x} \left\{ -p' u' + \frac{1}{Re} \frac{\partial}{\partial x} \left( \frac{1}{2} u'^2 \right) \right\} d\Omega}_{\text{Convection}} \\ &+ \underbrace{\int_S \frac{1}{Re} \left( -u' \frac{\partial v'}{\partial x} - u' f' \frac{\partial^2 \bar{u}_l}{\partial r^2} \right) dS}_{\text{Liquid viscous stress}} - \underbrace{\int_{\Omega} u' v' \frac{\partial \bar{u}}{\partial r} \, d\Omega}_{\text{Production}} \end{aligned}$$

$$\begin{aligned}
 & - \underbrace{\int_{\Omega} \frac{1}{Re} \left( \frac{\partial u'}{\partial x} \frac{\partial u'}{\partial x} + \frac{1}{r} \frac{\partial u'}{\partial \theta} \frac{1}{r} \frac{\partial u'}{\partial \theta} + \frac{\partial u'}{\partial r} \frac{\partial u'}{\partial r} \right) d\Omega}_{\text{Dissipation}} \\
 & + \underbrace{\int_{\mathcal{S}} \frac{1}{Re} m \left( u' \frac{\partial v'_g}{\partial x} + u' \frac{\partial u'_g}{\partial r} + u' f' \frac{\partial^2 \bar{u}_g}{\partial r^2} \right) d\mathcal{S}}_{\text{Gas viscous stress}}, \tag{4.3}
 \end{aligned}$$

$$\begin{aligned}
 & \int_{\Omega} \frac{D}{Dt} \left( \frac{1}{2} v'^2 \right) d\Omega \\
 & = \underbrace{\int_{\Omega} \frac{p'}{r} \frac{\partial}{\partial r} (rv') d\Omega}_{\text{Pressure-velocity correlation}} + \underbrace{\int_{\mathcal{S}} \left( -\eta p'_g v'_g + \frac{2m}{Re} v \frac{\partial v'_g}{\partial r} \right) d\mathcal{S}}_{\text{Gas viscous stress}} - \underbrace{\int_{\mathcal{S}} \frac{1}{Re} v' \frac{\partial v'}{\partial r} d\mathcal{S}}_{\text{Liquid viscous stress}} \\
 & - \underbrace{\int_{\Omega} \frac{1}{Re} \left( \frac{\partial v'}{\partial r} \frac{\partial v'}{\partial r} + \frac{1}{r} \frac{\partial v'}{\partial \theta} \frac{1}{r} \frac{\partial v'}{\partial \theta} + \frac{\partial v'}{\partial x} \frac{\partial v'}{\partial x} + \frac{v'^2}{r^2} + \frac{2}{r^2} v' \frac{\partial w'}{\partial \theta} \right) d\Omega}_{\text{Dissipation}} \\
 & + \underbrace{\int_{\Omega} \frac{1}{Re} \frac{\partial^2}{\partial x \partial x} \left( \frac{1}{2} v'^2 \right) d\Omega}_{\text{Convection}} - \underbrace{\int_{\mathcal{S}} \frac{1}{We} (-1 + n^2 + \alpha^2) f' v' d\mathcal{S}}_{\text{Surface tension energy}}, \tag{4.4}
 \end{aligned}$$

$$\begin{aligned}
 & \int_{\Omega} \frac{D}{Dt} \left( \frac{1}{2} w'^2 \right) d\Omega \\
 & = \underbrace{\int_{\Omega} \frac{p'}{r} \frac{\partial w'}{\partial \theta} d\Omega}_{\text{Pressure-velocity correlation}} + \underbrace{\int_{\Omega} \frac{1}{Re} \frac{\partial^2}{\partial x \partial x} \left( \frac{1}{2} w'^2 \right) d\Omega}_{\text{Convection}} + \underbrace{\int_{\mathcal{S}} \frac{1}{Re} \left( -w' \frac{\partial v'}{\partial \theta} - w'^2 \right) d\mathcal{S}}_{\text{Liquid viscous stress}} \\
 & - \underbrace{\int_{\Omega} \frac{1}{Re} \left( \frac{\partial w'}{\partial r} \frac{\partial w'}{\partial r} + \frac{1}{r} \frac{\partial w'}{\partial \theta} \frac{1}{r} \frac{\partial w'}{\partial \theta} + \frac{\partial w'}{\partial x} \frac{\partial w'}{\partial x} + \frac{w'^2}{r^2} - \frac{2}{r^2} w' \frac{\partial v'}{\partial \theta} \right) d\Omega}_{\text{Dissipation}} \\
 & + \underbrace{\int_{\mathcal{S}} \frac{1}{Re} m \left( w' \frac{\partial w'_g}{\partial r} + w' \frac{\partial v'_g}{\partial \theta} - w' w'_g \right) d\mathcal{S}}_{\text{Gas viscous stress}}. \tag{4.5}
 \end{aligned}$$

Unless marked by a subscript  $g$ , all quantities are evaluated in the liquid phase. In this context, we also note that the evolution of the surface tension energy is related to the surface tension term in the energy budget (4.6) as follows:

$$\int_{\mathcal{S}} \frac{D}{Dt} \left( \frac{1}{We} (-1 + n^2 + \alpha^2) f'^2 \right) d\mathcal{S} = 2 \int_{\mathcal{S}} \frac{1}{We} (-1 + n^2 + \alpha^2) f' v' d\mathcal{S}. \tag{4.6}$$



*A mechanism for the amplification of interface distortions*

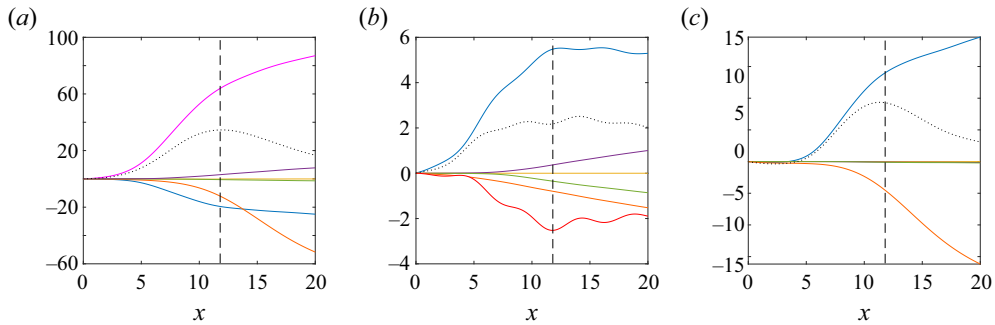


Figure 7. Evolution of the terms of the component-wise energy budgets. (a) Streamwise component. (b) Radial component. (c) Azimuthal component. Production (magenta), gas viscous stress (purple), liquid viscous stress (green), PVC (blue), surface tension energy (red), dissipation (orange) and convective (yellow) terms, and their sum (back dotted). The vertical dashed line marks the target location,  $x_1 = 11.8$ . The parameters are  $Re = 7500$ ,  $We = 3000$ ,  $m = 0.01$ ,  $\eta = 0.001$ ,  $n = 5$  and  $\omega = 2.2$ .

The evolution of the budget terms for the three velocity components from the initial location  $x = 0$  to the target location  $x_1 = 11.8$  is presented in figure 7. Consistent with the case considered in the previous section, the parameters are  $Re = 7500$ ,  $We = 3000$ ,  $m = 0.01$ ,  $\eta = 0.001$ ,  $n = 5$  and  $\omega = 2.2$ . Positive values indicate that the respective term introduces perturbation kinetic energy in the considered component while negative-valued terms extract perturbation kinetic energy from the component. The sum of all quantities at a given downstream location denotes the variation of perturbation kinetic energy in the corresponding component. Consistent with the considered optimization problem, the energy budgets are normalized by the total perturbation energy at the initial location,  $x = 0$ .

When considering the budget of the streamwise velocity component in figure 7(a), the production term is positive throughout the evolution of perturbation. This term acts as the main energy source of the perturbations by extracting energy from the mean shear. The gas viscous stress terms are of positive sign in both the streamwise and radial dimensions, although their magnitudes are small compared with the production term. In contrast, the dissipation terms are negative for all three components, meaning that energy is drained by viscous dissipation.

Of particular interest is the pressure–velocity correlation (PVC) term. The sum of the PVC terms of the individual velocity components is zero, and the PVC terms thus introduce an inter-component redistribution of perturbation energy. For the present case, the PVC term in the budget of the streamwise velocity component remains negative for the entire process, while positive values are observed for the radial component. In the azimuthal component, the PVC term is initially marginally negative, and eventually attains positive values for  $x \gtrsim 4$ . The PVC term thus drains energy from the streamwise component and reintroduces it into the radial and azimuthal components. In this manner, perturbation kinetic energy is introduced into the streamwise component by the mean shear, and transferred to the azimuthal and radial components via the PVC terms.

The surface tension energy term only appears in the budget of the radial component, (4.4), and the growth of the energy stored in the interface energy thus occurs independent of the budgets representing the streamwise and azimuthal components. The perturbation energy conveyed to the interface can therefore be studied by considering the interfacial stress condition, (2.30c). Multiplication by  $v'$  and integration along the liquid surface

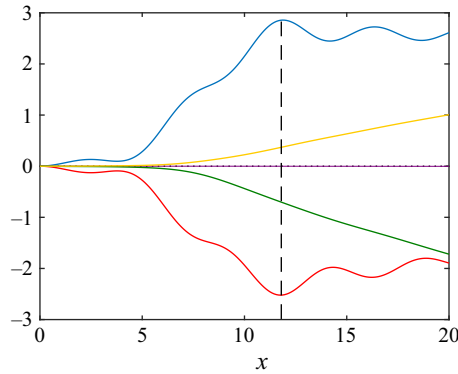


Figure 8. Evolution of the terms of the energy budget at the liquid jet interface. Liquid PVC (blue), gas viscous stress (yellow), liquid viscous stress (green), gas PVC (purple) and surface tension energy (red) terms, and their sum (black dotted line). The black dashed line marks the target location,  $x_1 = 11.8$ . The parameters are  $Re = 7500$ ,  $We = 3000$ ,  $m = 0.01$ ,  $\eta = 0.001$ ,  $n = 5$  and  $\omega = 2.2$ .

yields

$$\begin{aligned}
 & \underbrace{\int_S -p'_l v' dS}_{\text{Liquid pressure-velocity correlation}} + \underbrace{\int_S \frac{2}{Re} \left( v' \frac{\partial v'_l}{\partial r} \right) dS}_{\text{Liquid viscous stress}} + \underbrace{\int_S \eta p'_g v' dS}_{\text{Gas pressure-velocity correlation}} - \underbrace{\int_S \frac{2m}{Re} \left( v' \frac{\partial v'_g}{\partial r} \right) dS}_{\text{Gas viscous stress}} \\
 & + \underbrace{\int_S \frac{1}{We} (-1 + n^2 + \alpha^2) f' v' dS}_{\text{Surface tension energy}} = 0. \tag{4.7}
 \end{aligned}$$

The terms in (4.7) are presented in figure 8. The sum of all terms is zero at all downstream locations, and the gas PVC term is of negligible amplitude. Any gain in the surface perturbation energy can thus be attributed to the balance of the remaining three terms. The results show that the main source of energy is the liquid PVC term. During the early stages ( $x \leq 7$ ), the magnitude of the liquid PVC term effectively matches that of the energy absorbed by the surface tension energy while viscous stress terms are nearly zero. Past this point, the liquid PVC and the surface tension terms grow rapidly with matching oscillation patterns. In contrast, the viscous terms grow smoothly, again with matching trends in the two liquids. The positive contribution by the gas viscous stress is moderately exceeded by the negative contribution of the liquid viscous stress, with the difference being compensated by the liquid PVC term. The outcome establishes that the gain in surface tension energy is indeed driven by the liquid PVC term.

In summary, the discussion of the energy budget establishes the mechanics of the algebraic amplification of interface distortions. Perturbation kinetic energy is generated by the mean shear in the streamwise perturbation velocity component and transferred to the radial component through the PVC term. Since only the radial component is kinematically coupled to the interface displacement, this redistribution mechanism is critical in enabling the amplification of interface distortions. At the interface, the energy introduced by the PVC term acts as a source for increasing the surface tension energy.

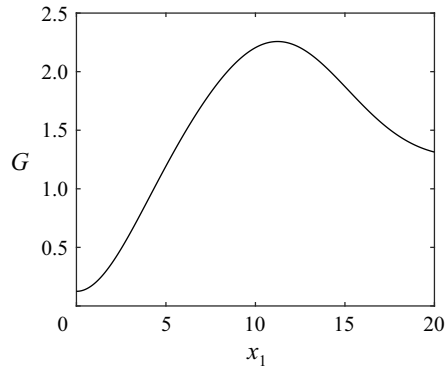


Figure 9. Energy gain  $G$  as a function of the target location  $x_1$ . The parameters are  $Re = 7500$ ,  $We = 3000$ ,  $m = 0.01$ ,  $\eta = 0.001$ ,  $\omega = 2.2$  and  $n = 5$ .

After the qualitative demonstration of the algebraic amplification of interface distortions, and the analysis of the underlying dynamics, we seek in the following to quantify the scaling of the mechanism with several key parameters.

### 5. Parameter influence and scaling

The considered problem is governed by five parameters: the Reynolds number  $Re$ , the Weber number  $We$ , the ratio of the densities of the two fluids  $\eta$ , the ratio of their viscosities  $m$  and the azimuthal wavenumber of the perturbations  $n$ . The frequency of the perturbations  $\omega$  and the target location  $x_1$  of the analysis of optimal disturbances describe two additional parameters in the determination of the gain  $G$ . As noted in § 2.5, these parameters are nonetheless eliminated in the consideration of the maximum gain  $G_{max}$  which is defined as the maximum of all  $G(\omega, x_1)$ . Following its definition in (2.50), the objective functional  $G$  relates the interface energy at the target location  $x_1$  to the sum of the kinetic and interface perturbation energies at the initial position  $x = 0$ . In other words,  $G$  quantifies the interface energy at  $x_1$  normalized by the total initial perturbation energy. In doing so, it defines a conservative measure for the gain of the interface energy that discounts the trivial redistribution of initial perturbation kinetic energy into surface tension energy at the target location. We note that a side effect of this approach is that the initial value of  $G$  at  $x = 0$  is in general not unity.

The influence of the target location  $x_1$  on the objective functional  $G$  is presented in figure 9. We note that the presented gain in surface tension energy at each target location is the result of an independent evaluation of the optimization problem. For example, the maximum  $G$  for the parameters  $Re = 7500$ ,  $We = 3000$ ,  $m = 0.01$ ,  $\eta = 0.001$ ,  $\omega = 2.2$  and  $n = 5$  is  $G = 2.638$  at  $x_1 = 11.8$  in figure 9.

In the remainder, we will focus on the maximum gain  $G_{max} = \max_{\omega, x_1} G(\omega, x_1)$  which is obtained by maximizing  $G$  for all possible combinations of  $\omega$  and  $x_1$ . The azimuthal wavenumber is chosen from the range of exponentially stable settings,  $n = \{5, 6, 7\}$ . We maintain a constant base flow and investigate the effect of the Reynolds and Weber numbers as well as the viscosity and density ratios of the two fluids on the amplification of perturbations.

An overview of the effect of the Reynolds and Weber numbers on  $G_{max}$  is presented in figure 10. The remaining parameters are kept constant at  $m = 0.01$ ,  $\eta = 0.001$  and  $n = 5$ . The effect of the Reynolds number is monotonic so that higher  $Re$  also leads to higher gain

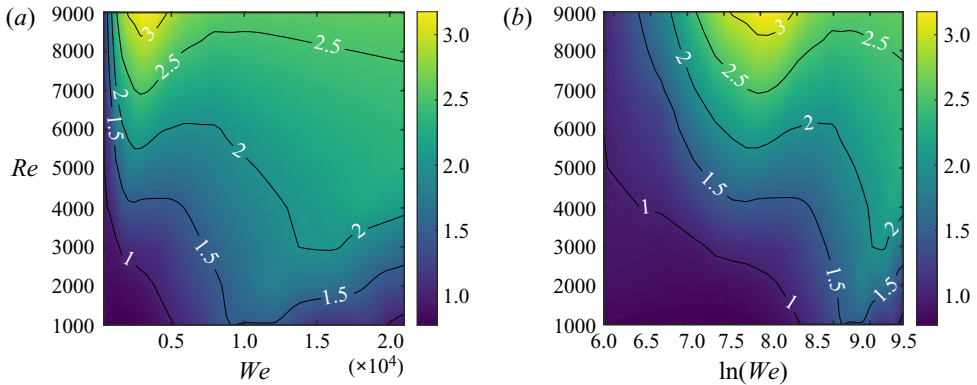


Figure 10. Contours of the maximum energy gain  $G_{max}$  as a function of the Reynolds number  $Re$  and the Weber number  $We$  (a) in linear scale and (b) in logarithmic scale. The parameters are  $m = 0.01$ ,  $\eta = 0.001$  and  $n = 5$ .

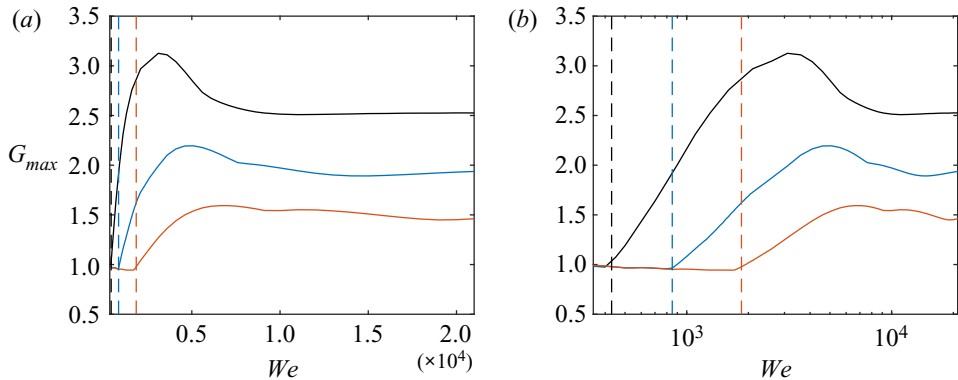


Figure 11. Energy gain  $G_{max}$  as a function of the Weber number  $We$  (a) in linear scale and (b) in logarithmic scale for  $n = 5$  (black),  $n = 6$  (blue) and  $n = 7$  (red). The critical Weber numbers  $We_c$  corresponding to  $G_{max} = 1$  are marked by dashed lines. The parameters are  $Re = 9000$ ,  $m = 0.01$  and  $\eta = 0.001$ .

of the objective functional. On the other hand, an increase of the Weber number leads to a local maximum in  $G_{max}$ , with further increases of  $We$  reducing the gain. More generally speaking, the presented result establishes that both viscosity and surface tension have an appreciable effect on the amplification of interface distortions.

The influence of the Weber number at fixed  $Re = 9000$  is isolated in figure 11 for three different azimuthal numbers. In all cases,  $G_{max}$  is initially marginally below 1, followed by a sharp increase that leads to a local maximum which tends to have larger magnitude at smaller  $n$ . A further increase of the Weber number causes  $G_{max}$  to decrease before remaining approximately constant for a comparatively large range of Weber numbers. Since the numerator of  $G$  is proportional to  $f$  and  $\sigma$ , and thus the inverse of the Weber number, this result implies that the magnitude of the surface distortion grows with  $We$ .

Analogously, we investigate the scaling of  $G_{max}$  with the Reynolds number at constant Weber number. The resulting  $G_{max}$  for a density ratio  $m = 0.01$  and a viscosity ratio  $\eta = 0.001$  is presented in figures 12 and 13. We focus on two different regimes, the first relating to the local maximum of  $G_{max}$  at relatively low Weber number seen in figure 11. The three considered cases are  $n = 5$  at  $We = 3000$ ,  $n = 6$  at  $We = 5000$  and  $n = 7$  at

A mechanism for the amplification of interface distortions

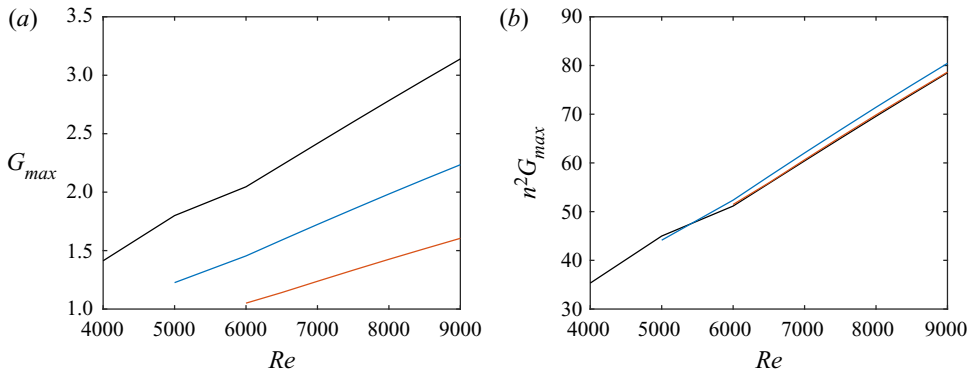


Figure 12. Amplification ratio  $G_{max}$  as a function of the Reynolds number  $Re$  at the local maximum in terms of the Weber number: (a)  $G_{max}$  and (b)  $n^2 G_{max}$ . Azimuthal wavenumbers  $n = 5$ ,  $We \sim 3000$  (black);  $n = 6$ ,  $We \sim 5000$  (blue); and  $n = 7$ ,  $We \sim 6000$  (red). The parameters are  $m = 0.01$  and  $\eta = 0.001$ .

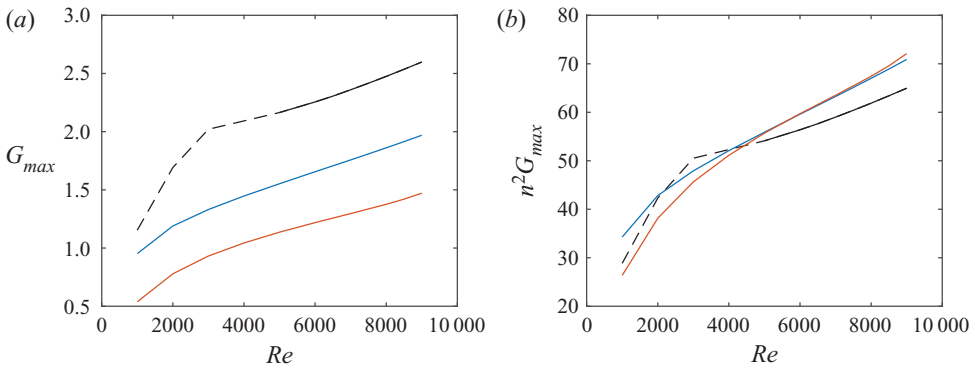


Figure 13. Amplification ratio  $G_{max}$  as a function of the Reynolds number  $Re$  in the regime of relatively high Weber number: (a)  $G_{max}$  and (b)  $n^2 G_{max}$ . Azimuthal wavenumbers  $n = 5$  (black),  $n = 6$  (blue) and  $n = 7$  (red). The parameters are  $We = 20\,000$ ,  $m = 0.01$  and  $\eta = 0.001$ .

$We = 6000$ . The scaling of  $G_{max}$  with the Reynolds number is presented in figure 12(a) for three azimuthal wavenumbers. Within the considered range of Reynolds numbers,  $G_{max}$  linearly increases with  $Re$ . The slope of the lines nonetheless decreases with  $n$ . When pre-multiplied with the square of the azimuthal wavenumber  $n$ , the different lines effectively collapse (see figure 12b). The result thus establishes that the peak  $G_{max}$  scales as

$$G_{max} \sim \frac{Re}{n^2}. \quad (5.1)$$

The second regime is related to the region of near-constant  $G_{max}$  at relatively high  $We$ . For  $We = 20\,000$ ,  $G_{max}$  again grows linearly with the Reynolds number for sufficiently large  $Re$  (see figure 13a). As demonstrated in figure 13(b), the inverse proportionality of  $G_{max}$  to the square of the azimuthal wavenumber does not, however, extend to the regime of higher Weber numbers.

Overall, the results establish a linear scaling of  $G_{max}$  with the Reynolds number throughout the considered range of Weber numbers. The differing scaling with the azimuthal wavenumber depending on the Weber number nonetheless points to differences in the evolution of the perturbation flow field. These differences are qualitatively illustrated

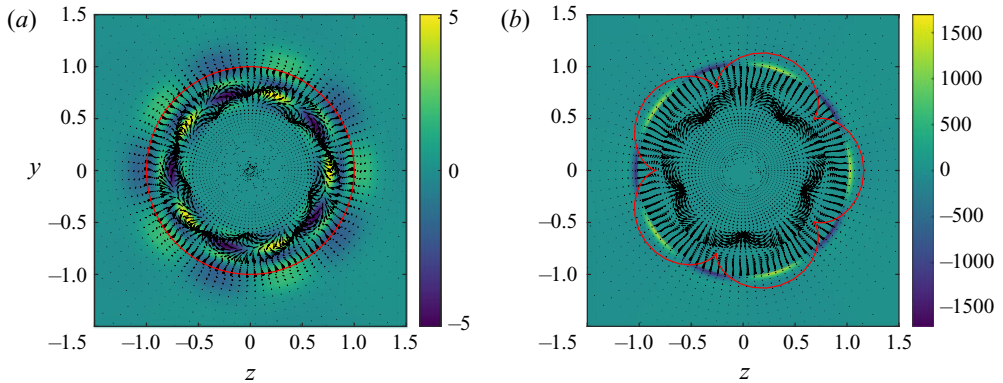


Figure 14. Cross-planes showing (a) the optimal initial condition at  $x_0 = 0$  and (b) its evolution at  $x_1 = 11.8$ . Vectors of the radial and azimuthal disturbance fields,  $v'$  and  $w'$ , with colour contours of streamwise disturbance field,  $u'$ . The red line marks the position of the material interface. The parameters are  $Re = 7500$ ,  $We = 3000$ ,  $m = 0.01$ ,  $\eta = 0.001$ ,  $n = 5$  and  $\omega = 2.2$ .

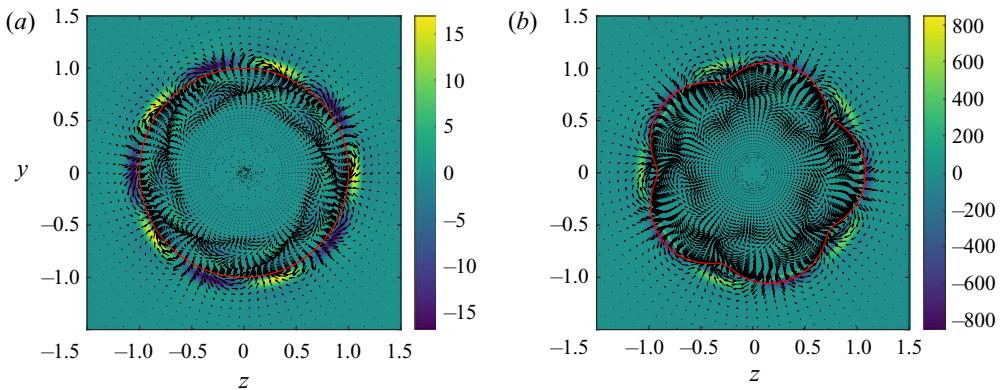


Figure 15. Cross-planes showing (a) the optimal initial condition at  $x_0 = 0$  and (b) its evolution at  $x_1 = 11.2$ . Vectors of the radial and azimuthal disturbance fields,  $v'$  and  $w'$ , with colour contours of streamwise disturbance field,  $u'$ . The red line marks the position of the material interface. The parameters are  $Re = 7500$ ,  $We = 10000$ ,  $m = 0.01$ ,  $\eta = 0.001$ ,  $n = 5$  and  $\omega = 1.7$ .

by the perturbation fields in cross-planes at both the initial and final locations between the cases of low and high Weber number (see figures 14 and 15). At low Weber number, the highest perturbation amplitudes in the radial velocity component at the target location occur within the jet, at approximately two-thirds of the jet radius. In contrast, the most intense fluctuations at comparatively high  $We$  are observed at the interface location.

We now turn to examining the effect of the viscosity ratio  $m$  and the density ratio  $\eta$  on the amplification mechanism. We maintain a tractable problem by keeping the remainder of the parameter space at constant values,  $Re = 6000$ ,  $We = 1000$  and  $n = 5$ . Contours in figure 16 present the maximum surface tension energy gain  $G_{max}$  for the range  $0.01 \leq m \leq 0.335$  and  $0.001 \leq \eta \leq 0.08$ . We note that the viscosity ratio determines the ratio of the thicknesses of the shear layers in the two fluids, with higher values of  $m$  corresponding to a relatively thicker shear layer in the gas phase. Moreover, the density ratio is related to the ratio of the perturbation kinetic energy in the two phases. The result shows that the growth

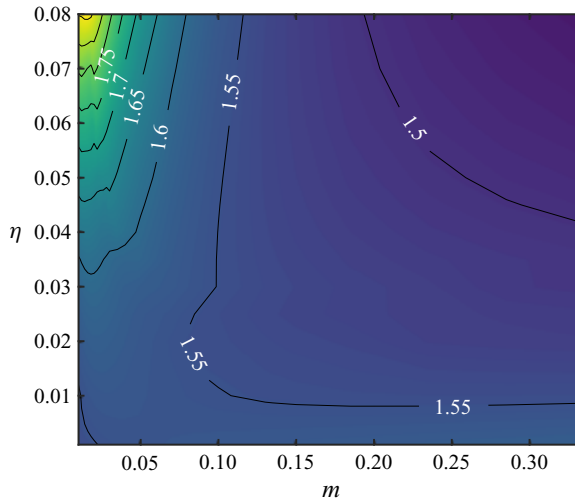


Figure 16. Contours of the energy gain  $G_{max}$  as a function of the viscosity ratio  $m$  and the density ratio  $\eta$ . The parameters are  $Re = 6000$ ,  $We = 1000$  and  $n = 5$ .

of the interface distortion is highest for a combination of comparatively low viscosity ratio and high density ratio.

The results presented in figures 10 and 11 established that for small Weber numbers, the objective functional remains marginally below unity before rising sharply once a certain threshold for  $We$  is exceeded. In this context, we recall that the definition of the objective functional implies that for  $G_{max} < 1$ , the perturbation surface tension energy at the target location is less than the total perturbation energy at the initial position, implying either passive decay or a trivial redistribution of initial perturbation kinetic energy into the interface. On the other hand, for cases with  $G_{max} > 1$ , the perturbation interface energy at the target position exceeds the total perturbation energy at the initial position, which implies that energy has been extracted from the mean shear and converted into surface tension energy.

In the following, we seek to characterize the critical Weber number  $We_c$  at which  $G_{max}$  crosses unity, and which thus marks the boundary at which the distortion to the material interface grows in a non-trivial manner by means of a redistribution of energy from the mean shear. In terms of the energy budget, this implies that the right-hand side of (4.4) yields a positive value so that the contribution to the perturbation kinetic energy by the radial component at the target location  $x_1$  has increased compared to the initial location  $x_0$ . The difference in the kinetic energy in the radial velocity component between the initial and target locations,  $\Delta \frac{1}{2} v'^2 = \frac{1}{2} (v'^2(x_1) - v'^2(0))$ , is presented in figure 18(a). The Weber numbers at which each of the curves crosses zero coincide with the critical Weber numbers identified in figure 11.

In the exploration of a potential scaling law for the critical Weber number, we turn to the critical Ohnesorge number,

$$Oh_c = \frac{\sqrt{We_c}}{Re}, \quad (5.2)$$

which relates the viscous forces to the inertial and surface tension forces at the critical Weber number. Figure 17 shows the logarithm of the Ohnesorge number,  $\ln(Oh_c)$ , for the corresponding critical Weber number as a function of the logarithm of the

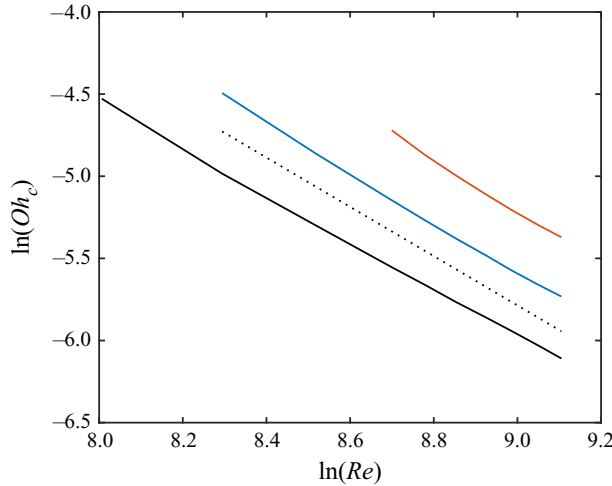


Figure 17. Scaling of the logarithm of the critical Ohnesorge number  $Oh_c$  with the logarithm of the Reynolds number  $Re$ . Here  $n = 5$  (black),  $n = 6$  (blue) and  $n = 7$  (red). The parameters are  $m = 0.01$  and  $\eta = 0.001$ . The black dotted line indicates a reference slope of  $-3/2$ .

Reynolds number. A linear trend is observed with a slope of approximately  $-3/2$ , suggesting that  $Oh_c \sim Re^{-3/2}$ .

Insight into the scaling of  $Oh_c$  and thus  $We_c$  is gained by extending the analysis of the energy budget presented in the preceding section, where it was shown that the PVC term is the major source of the surface tension energy. Since the measure for the gain of the interface energy  $G$  relates the surface tension energy at a certain downstream location  $x_1$  to the initial total energy of the perturbation, it follows that  $G$  is proportional to the PVC term in (4.7). Previous results in figure 12(a) further showed that  $G$  scales with  $Re$ . Thus,

$$\int_{\Omega} \frac{p'}{r} \frac{\partial}{\partial r} (rv') \, d\Omega \approx C_1 Re, \quad \text{with } C_1 \geq 0. \tag{5.3}$$

For the considered cases,  $n^2 \gg 1$ , and also  $n^2 \gg \alpha^2$ . The surface tension energy term is thus approximated as

$$\int_S \frac{1}{We} \left(-1 + n^2 + \alpha^2\right) f' v' \, dS \approx \frac{C_2}{We}, \quad \text{with } C_2 \geq 0. \tag{5.4}$$

Using the energy budget in the radial velocity component (4.4), the condition at the critical Weber number of  $\Delta \frac{1}{2} v^2 \geq 0$  becomes

$$\begin{aligned} & \int_{\Omega} \frac{p'}{r} \frac{\partial}{\partial r} (rv') \, d\Omega + \int_S \left( -\eta p'_g v'_g + \frac{2m}{Re} v' \frac{\partial v'_g}{\partial r} \right) dS \\ & - \int_S \frac{1}{Re} v' \frac{\partial v'}{\partial r} \, dS + \int_{\Omega} \frac{1}{Re} \frac{\partial^2}{\partial x \partial x} \left( \frac{1}{2} v^2 \right) d\Omega + \int_S \frac{1}{We} \left(-1 + n^2 + \alpha^2\right) f' v' \, dS \\ & - \int_{\Omega} \frac{1}{Re} \left( \frac{\partial v'}{\partial r} \frac{\partial v'}{\partial r} + \frac{1}{r} \frac{\partial v'}{\partial \theta} \frac{1}{r} \frac{\partial v'}{\partial \theta} + \frac{\partial v'}{\partial x} \frac{\partial v'}{\partial x} + \frac{v^2}{r^2} + \frac{2}{r^2} v' \frac{\partial w'}{\partial \theta} \right) d\Omega \geq 0. \end{aligned} \tag{5.5}$$



Substitution of (5.3) and (5.4) into (5.5) yields

$$C_1 Re \geq \frac{C_2}{We} + \frac{C_3}{Re}, \quad (5.6)$$

with  $C_3$  defined as

$$C_3 = \int_S \left( \eta p'_g v'_g - 2mv' \frac{\partial v'_g}{\partial r} \right) dS + \int_S v' \frac{\partial v'}{\partial r} dS - \int_\Omega \frac{\partial^2}{\partial x \partial x} \left( \frac{1}{2} v'^2 \right) d\Omega \\ + \int_\Omega \left( \frac{\partial v'}{\partial r} \frac{\partial v'}{\partial r} + \frac{1}{r} \frac{\partial v'}{\partial \theta} \frac{1}{r} \frac{\partial v'}{\partial \theta} + \frac{\partial v'}{\partial x} \frac{\partial v'}{\partial x} + \frac{v'^2}{r^2} + \frac{2}{r^2} v' \frac{\partial w'}{\partial \theta} \right) d\Omega. \quad (5.7)$$

The results in figure 8 showed that  $C_3$  is small compared to the PVC and surface tension energy terms, especially in the early stage of the evolution, and thus  $C_3 \ll C_1, C_2$ . Hence, for  $Re \gg 1$ , we obtain

$$C_1 Re^3 \geq C_2 \frac{Re^2}{We_c}, \quad (5.8)$$

so that

$$Oh_c \geq C_4 Re^{-3/2}, \quad (5.9)$$

where  $C_4 = C_2/C_1$ . The predicted exponent of  $-3/2$  recovers the scaling observed in figure 17 and thus substantiates the power-law relation between the Reynolds number and the critical Ohnesorge number. Substitution of (5.2) yields the associated critical Weber number:

$$We_c \geq \frac{C_4^2}{Re}. \quad (5.10)$$

For Weber numbers below the critical value,  $We < We_c$ , the energy gain attains values less than unity, and the surface tension energy gain may thus be attributed to a redistribution of the initial perturbation kinetic energy without meaningful extraction of energy from the mean shear. In this regime, the target location  $x_1$  at which  $G_{max}$  is attained is expected to be comparatively close to the initial position  $x = 0$  so as to minimize any losses of perturbation kinetic energy due to viscous dissipation. Results presented in figure 18(b) showing the target location  $x_1$  as a function of Weber number confirm this hypothesis. For all considered azimuthal wavenumbers, the critical Weber numbers  $We_c$  coincide with an abrupt downstream shift of the target locations.

## 6. Nonlinear simulation

So far, we have demonstrated the algebraic mechanism for generating interface distortion exclusively by means of linear analyses. In this setting, the nonlinear higher-order terms in the governing equation are neglected which in turn allows the identification of optimal solutions in the interface energy norm as combinations of the non-orthogonal eigenfunctions. In the following, we demonstrate the realizability of the identified mechanism in a nonlinear setting by means of a simulation of the full two-fluid Navier–Stokes equations.

The nonlinear simulations employ the Basilisk solver (Popinet 2015, 2018) which is based on a conservative, non-diffusive geometric volume-of-fluid scheme to track the material interface. The evolution of the interface is captured by advecting a

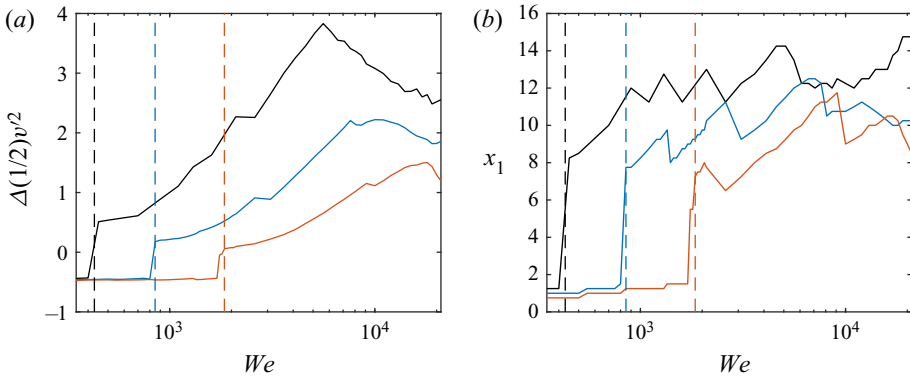


Figure 18. (a) Perturbation kinetic energy gain in the radial direction,  $\Delta\frac{1}{2}v^2$ , as a function of Weber number  $We$ . (b) Target location  $x_1$  as a function of Weber number. Azimuthal wavenumbers  $n = 5$  (black),  $n = 6$  (blue) and  $n = 7$  (red). The parameters are  $Re = 9000$ ,  $m = 0.01$  and  $\eta = 0.001$ . Dashed lines mark the critical Weber numbers  $We_c$ .

volume-fraction function coupled with the incompressible Navier–Stokes equations. An orthogonally structured grid of size  $[N_x, N_y, N_z] = [1536 \times 256 \times 256]$  and spatial extent  $[L_x, L_y, L_z] = [60R, 10R, 10R]$  is used. In this setting, the radius of the jet is defined as  $r = (y^2 + z^2)^{1/2}$  in the  $y$ – $z$  plane. A homogeneous uniform grid spacing of  $\Delta x = 0.004$  is applied in all dimensions. We note that the comparatively large streamwise extent of the computational domain prevents any interaction of the jet with the outflow plane during the runtime of the simulations.

In a first step, a base flow is computed by imposing the profile (2.2) at the inflow of the computational domain. After the initial transient has cleared, the base flow profile is superimposed with the optimal initial condition identified in the solution of the optimization problem (3.1) for the parameters  $Re = 7784$ ,  $We = 4865$ ,  $m = 0.036$ ,  $\eta = 0.0012$ ,  $n = 6$  and  $\omega = 2.5$ . Homogeneous Neumann boundary conditions are imposed on both the side walls and the outlet:

$$\left. \begin{aligned} \frac{\partial \mathbf{u} \cdot \hat{\mathbf{e}}_n}{\partial n} &= 0 & \text{if } \frac{\partial \mathbf{u} \cdot \hat{\mathbf{e}}_n}{\partial n} > 0, \\ \mathbf{u} \cdot \hat{\mathbf{e}}_n &= 0 & \text{otherwise,} \end{aligned} \right\} \quad (6.1)$$

where  $\hat{\mathbf{e}}_n$  is the face-normal vector pointing outward of the domain. The convergence of the simulation results was verified by increasing the resolution as well as changing the domain size in the  $y$  and  $z$  directions.

An isosurface of the material interface at time  $t = 0.24$  is presented in figure 19(a). Colours indicate the local amplitude of the interface distortion. The linear result, rescaled to the same initial amplitude of the perturbations, is presented in figure 19(b) and shows excellent qualitative agreement.

The envelopes of the amplitudes of the interface perturbations computed in linear analysis and the nonlinear simulations are plotted in figure 20. The nonlinear simulation qualitatively recovers the non-monotonic growth of the perturbation observed in the linear analysis. In both cases, the global maximum is preceded by two local maxima past which the amplitude of the interface distortion decays before amplifying again. The prediction by linear theory and the nonlinear simulation are in excellent agreement in the vicinity of the nozzle. With growing distance to the exit of the nozzle, a moderate discrepancy between the two results appears. The peak amplitude of the interface distortion is recorded at

*A mechanism for the amplification of interface distortions*

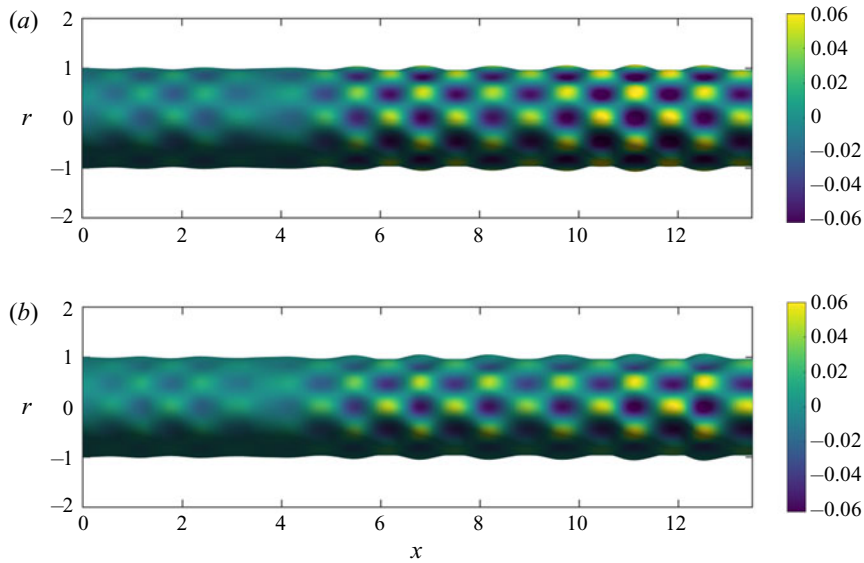


Figure 19. Isosurfaces of the material interface, coloured by the local displacement of the interface. (a) Linear stability theory. (b) Nonlinear simulation based on a geometric volume-of-fluid formulation. The parameters are  $Re = 7784$ ,  $We = 4865$ ,  $m = 0.036$ ,  $\eta = 0.0012$ ,  $n = 6$  and  $\omega = 2.5$ .

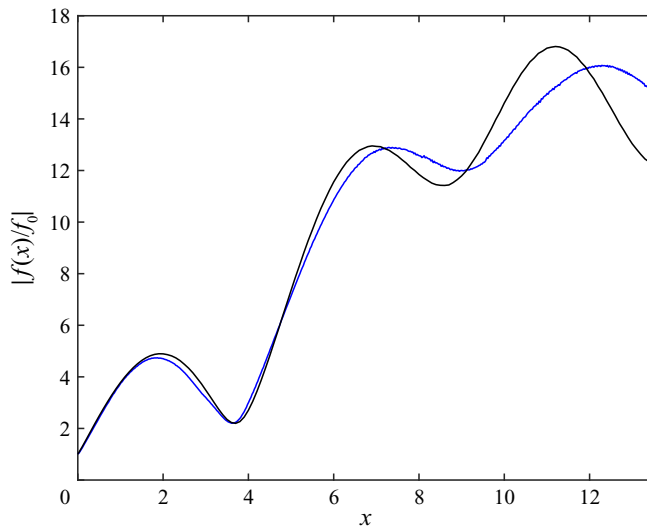


Figure 20. Envelope of the interface distortion of the liquid jet. Linear stability theory (black) and nonlinear simulation based on a geometric volume-of-fluid formulation (blue). The parameters are  $Re = 7784$ ,  $We = 4865$ ,  $m = 0.036$ ,  $\eta = 0.0012$ ,  $n = 6$  and  $\omega = 2.5$ .

$x = 11.2$  in the linear analysis while it is located at  $x = 12.37$  in the nonlinear simulation. The magnitude of the maximum interface distortion also attains a moderately lower value of  $|f(x)/f_0| = 16.05$  in the nonlinear simulation, compared to a value of  $|f(x)/f_0| = 16.81$  predicted in the linear analysis. This disparity can be attributed to the relaxation of the base flow in the nonlinear simulation which leads to a thickening of the shear layer with increasing distance to the inflow location at  $x = 0$ . In contrast, the linear analysis assumes a constant base flow profile which matches that at the inflow location of the

nonlinear simulation. An evaluation of the surface tension energy gain  $G_{max}$  for the relaxed base flow at  $x = 10$  results in a reduced amplification ratio,  $|f(x)/f_0| = 14.08$ . Overall, the qualitative agreement between linear analysis and nonlinear simulations clearly substantiates the realizability of the presented mechanism.

## 7. Conclusions

The literature on two-fluid flows commonly ascribes the amplification of small interface distortions to exponential mechanisms that are driven by shear or surface tension effects. Our work presents an alternative pathway for the amplification of disturbances to the material interface of a liquid jet. Depending on the parameters, the mechanism can intensify small perturbations by several orders of magnitude, and on a faster scale than exponential mechanisms such as the K–H instability.

The analysis is based on the application of linear stability theory in a spatial framework which incorporates the viscosity of both phases as well as the surface tension at the material interface. A linear optimization problem identifies the particular initial condition that most effectively amplifies the magnitude of the distortion to the material interface. The formulation is cast in a manner that discounts the trivial redistribution of initial perturbation kinetic energy into perturbation surface tension energy, and maximizes the actual redistribution of energy from the mean shear into the distortion of the material interface. The approach differs from earlier analyses of non-exponential growth in two-fluid settings which commonly applied a norm based on the kinetic energy of the disturbances.

The most effective disturbances are related to the Orr mechanism and appreciably amplify the magnitude of the initial interface perturbation. The underlying principle is the reorientation of initially tilted structures by the mean shear. Since the Orr mechanism amplifies velocity perturbations both parallel and perpendicular to the direction of the mean shear, it enables the amplification of the distortions to the material interface which are kinematically coupled to velocity perturbations in the radial component only. Analyses of the energy budget illustrated that perturbation energy is extracted from the mean shear by the production term of the streamwise perturbation velocity component. The PVC term redistributes the energy from the streamwise component into the radial component where it is transferred into surface tension energy in the form of a distortion to the material interface.

The surface tension energy gain was shown to scale linearly with the Reynolds number. The critical Weber number past which the surface tension energy in the material interface at the final location exceeds the initial total perturbation energy was related to the Reynolds number through a power law. Simulations of the full multi-phase Navier–Stokes equations confirmed the realizability of the mechanism and quantitatively verified the outcome of the linear analyses.

The presented mechanism may participate in the primary atomization process of liquid jets by providing a route for the shear-driven amplification of initial distortions to the material interface. The identification and comparison of its efficacy in triggering the secondary instabilities which further advance the flow towards breakup remain a subject of future research. We finally note that similar physics may also be relevant in the case of planar interfaces.

**Funding.** H.H. is funded by the Franklin P. and C.M. Johnson Fellowship and by the United States Department of Energy under the Predictive Science Academic Alliance Program 2 (PSAAP2) at Stanford University.

**Declaration of interests.** The authors report no conflict of interest.

Author ORCIDs.

 Hanul Hwang <https://orcid.org/0000-0002-0743-1925>;

 Parviz Moin <https://orcid.org/0000-0002-0491-7065>;

 M.J. Philipp Hack <https://orcid.org/0000-0001-9308-5397>.

Appendix A. Linear operators

The system matrices  $\mathbf{M}$  and  $\mathbf{L}$  in (2.31) are

$$\mathbf{M} = \begin{bmatrix} \tilde{\mathbf{M}}_j & 0 & 0 & 0 \\ 0 & \bar{u}^I & 0 & 0 \\ 0 & -i & 0 & 0 \\ 0 & 0 & 0 & \tilde{\mathbf{M}}_j \end{bmatrix}, \tag{A1}$$

$$\mathbf{L} = \begin{bmatrix} \tilde{\mathbf{L}}_j & 0 & 0 & 0 \\ 0 & i\omega & 0 & \mathbf{L}^I \\ 0 & 0 & 1 & 0 \\ 0 & 0 & 0 & \tilde{\mathbf{L}}_j \end{bmatrix}, \tag{A2}$$

with the block matrices  $\tilde{\mathbf{M}}_j$ ,  $\tilde{\mathbf{L}}_j$  and  $\mathbf{L}^I$  defined as

$$\tilde{\mathbf{M}}_j = \begin{bmatrix} \bar{u}_j & 0 & 0 & 1 & -\frac{i}{Re_j} & 0 & 0 \\ 0 & \bar{u}_j & 0 & 0 & 0 & -\frac{i}{Re_j} & 0 \\ 0 & 0 & \bar{u}_j & 0 & 0 & 0 & -\frac{i}{Re_j} \\ 1 & 0 & 0 & 0 & 0 & 0 & 0 \\ -i & 0 & 0 & 0 & 0 & 0 & 0 \\ 0 & -i & 0 & 0 & 0 & 0 & 0 \\ 0 & 0 & -i & 0 & 0 & 0 & 0 \end{bmatrix}, \tag{A3}$$

$$\tilde{\mathbf{L}}_j = \begin{bmatrix} \mathcal{U}_j & -i\frac{d\bar{u}_j}{dr} & 0 & 0 & 0 & 0 & 0 \\ 0 & \mathcal{V}_j & -\frac{i}{Re_j}\frac{2n}{r^2} & -\frac{d}{dr} & 0 & 0 & 0 \\ 0 & \frac{1}{Re_j}\frac{2n}{r^2} & \mathcal{W}_j & -i\frac{n}{r} & 0 & 0 & 0 \\ 0 & \mathcal{P}_j & -\frac{n}{r} & 0 & 0 & 0 & 0 \\ 0 & 0 & 0 & 0 & 1 & 0 & 0 \\ 0 & 0 & 0 & 0 & 0 & 1 & 0 \\ 0 & 0 & 0 & 0 & 0 & 0 & 1 \end{bmatrix} \tag{A4}$$

and

$$\mathbf{L}^I = [0 \ i \ 0 \ 0 \ 0 \ 0 \ 0]. \tag{A5}$$

The elements of the matrices  $\tilde{\mathbf{L}}_j$  are

$$U_j = \frac{1}{Re_j} \frac{\partial^2}{\partial r^2} + \frac{1}{Re_j} \frac{1}{r} \frac{\partial}{\partial r} + i\omega - \frac{1}{Re_j} \frac{n^2}{r^2}, \tag{A6}$$

$$V_j = \frac{1}{Re_j} \frac{\partial^2}{\partial r^2} + \frac{1}{Re_j} \frac{1}{r} \frac{\partial}{\partial r} + i\omega - \frac{1}{Re_j} \frac{n^2 + 1}{r^2}, \tag{A7}$$

$$W_j = \frac{1}{Re_j} \frac{\partial^2}{\partial r^2} + \frac{1}{Re_j} \frac{1}{r} \frac{\partial}{\partial r} + i\omega - \frac{1}{Re_j} \frac{n^2 + 1}{r^2}, \tag{A8}$$

$$P_j = \frac{\partial}{\partial r} + \frac{1}{r}. \tag{A9}$$

Note that the Reynolds numbers in (A6)–(A8) are related through  $Re_g = (\eta/m)Re_l$ .

### Appendix B. Interface energy norm

The interface energy owing to surface tension is defined as

$$E_{interface} = \int_0^\lambda \int_0^{2\pi/n} \sigma \gamma f \, dS, \tag{B1}$$

where  $\kappa$  is the the curvature of the interface. We further introduce the level-set function  $H$  as

$$H = r - f(x, \theta) = r - \left(1 + \hat{f} \exp(i(\alpha x + n\theta - \omega t))\right). \tag{B2}$$

The curvature of the liquid interface may then be expressed in terms of  $H$  as

$$\nabla H = \frac{\partial H}{\partial r} \mathbf{e}_r + \frac{1}{r} \frac{\partial H}{\partial \theta} \mathbf{e}_\theta + \frac{\partial H}{\partial x} \mathbf{e}_x = \mathbf{e}_r - \frac{in}{r} f \mathbf{e}_\theta - i\alpha f \mathbf{e}_x. \tag{B3}$$

Application of the Laplacian on  $H$  yields

$$\nabla^2 H = \frac{1}{r} \frac{\partial}{\partial r} \left( r \frac{\partial H}{\partial r} \right) + \frac{1}{r^2} \frac{\partial^2 H}{\partial \theta^2} + \frac{\partial^2 H}{\partial x^2} = \frac{1}{r} - \frac{n^2}{r^2} f - \alpha^2 f. \tag{B4}$$

Furthermore, the infinitesimal surface area  $dS$  is

$$dS = \left\{ 1 + \left( \frac{\partial f}{\partial \theta} \right)^2 + \left( \frac{\partial f}{\partial x} \right)^2 \right\}^{1/2} = |\nabla H| \, dx \, d\theta. \tag{B5}$$

Substitution of (B3)–(B5) into (B1) yields

$$\begin{aligned} E_{interface} &= \int_0^\lambda \int_0^{2\pi/n} \sigma \gamma f \, dS = \int_0^\lambda \int_0^{2\pi/n} \sigma \nabla \cdot \left( \frac{\nabla H}{|\nabla H|} \right) f |\nabla H| \, d\theta \, dx \\ &= \int_0^\lambda \int_0^{2\pi/n} \sigma \left( -f + \frac{n^2}{r^2} f + \alpha^2 f \right) f \, d\theta \, dx \\ &= \int_0^\lambda \int_0^{2\pi/n} \sigma \left( -1 + n^2 + \alpha^2 \right) f^2 \, d\theta. \end{aligned} \tag{B6}$$

## A mechanism for the amplification of interface distortions

### REFERENCES

- BAGUE, A., FUSTER, D., POPINET, S., SCARDOVELLI, R. & ZALESKI, S. 2010 Instability growth rate of two-phase mixing layers from a linear eigenvalue problem and an initial-value problem. *Phys. Fluids* **22** (9), 092104.
- BORONIN, S.A., HEALEY, J.J. & SAZHIN, S.S. 2013 Non-modal stability of round viscous jets. *J. Fluid Mech.* **716** (11), 96–119.
- BUTLER, K. & FARRELL, B.F. 1992 Three-dimensional optimal perturbations in viscous shear flow. *Phys. Fluids A* **4** (8), 1637–1650.
- CHIGIER, N. & EROGLU, H. 1989 Atomization of liquid jets from injection element in liquid rocket combustion chamber. *Second Quarterly Report to NASA*.
- CRUZ-MAZO, F., HERRADA, M.A., GAÑÁN-CALVO, A.M. & MONTANERO, J.M. 2017 Global stability of axisymmetric flow focusing. *J. Fluid Mech.* **832**, 329–344.
- DUDA, J.L. & VRENTAS, J.S. 1967 Fluid mechanics of laminar liquid jets. *Chem. Engng Sci.* **22** (6), 855–869.
- FARRELL, B. 1987 Developing disturbances in shear. *J. Atmos. Sci.* **44** (16), 2191–2199.
- FOURES, D.P.G., CAULFIELD, C.P. & SCHMID, P.J. 2012 Variational framework for flow optimization using seminorm constraints. *Phys. Rev.* **86**, 026306.
- FUSTER, D., MATAS, J.-P., MARTY, S., POPINET, S., HOEPPFNER, J., CARTELLIER, A. & ZALESKI, S. 2013 Instability regimes in the primary breakup region of planar coflowing sheets. *J. Fluid Mech.* **736**, 150–176.
- GONZÁLEZ-MENDIZABAL, D., OLIVERA-FUENTES, C. & GUZMÁN, J.M. 1987 Hydrodynamics of laminar liquid jets, experimental study and comparison with two models. *Chem. Engng Commun.* **56**, 117–137.
- GUSTAVSSON, L.H. 1991 Energy growth of three-dimensional disturbances in plane Poiseuille flow. *J. Fluid Mech.* **224** (1), 241–260.
- HACK, M.J.P. & MOIN, P. 2017 Algebraic disturbance growth by interaction of Orr and lift-up mechanisms. *J. Fluid Mech.* **829**, 112–126.
- HACK, M.J.P. & ZAKI, T.A. 2015 Modal and non-modal stability of boundary layers forced by spanwise wall oscillations. *J. Fluid Mech.* **778**, 389–427.
- HINCH, E.J. 1984 A note on the mechanism of the instability at the interface between two shearing fluids. *J. Fluid Mech.* **144**, 463–465.
- HOYT, J.W. & TAYLOR, J.J. 1977 Waves on water jets. *J. Fluid Mech.* **83** (1), 119–127.
- KHORRAMI, M.R., MALIK, M.R. & ASH, R.L. 1989 Application of spectral collocation techniques to the stability of swirling flows. *J. Comput. Phys.* **81** (1), 206–229.
- LANDAHL, M.T. 1975 Wave breakdown and turbulence. *SIAM J. Appl. Maths* **28** (4), 735–756.
- LANDAHL, M.T. 1980 A note on an algebraic instability of inviscid parallel shear flows. *J. Fluid Mech.* **98** (2), 243–251.
- LIN, S.P. & CHEN, J.N. 1998 Role played by the interfacial shear in the instability mechanism of a viscous liquid jet surrounded by a viscous gas in a pipe. *J. Fluid Mech.* **376**, 37–51.
- LIN, S.P. & IBRAHIM, E.A. 1990 Instability of a viscous liquid jet surrounded by a viscous gas in a vertical pipe. *J. Fluid Mech.* **218**, 641–658.
- LOZANO, A., BARRERAS, F., HAUKE, G. & DOPAZO, C. 2001 Longitudinal instabilities in an air-blasted liquid sheet. *J. Fluid Mech.* **437**, 143–173.
- MALIK, S.V. & HOOPER, A.P. 2007 Three-dimensional disturbances in channel flows. *Phys. Fluids* **19** (5), 052102.
- MARMOTTANT, P. & VILLERMAUX, E. 2004 On spray formation. *J. Fluid Mech.* **498**, 73–111.
- ORR, W.M.F. 1907 The stability or instability of the steady motions of a perfect liquid and of a viscous liquid. Part II: a viscous liquid. *Proc. R. Irish Acad.* **27**, 9–68.
- POPINET, S. 2015 A quadtree-adaptive multigrid solver for the Serre-Green-Naghdi equations. *J. Comput. Phys.* **302**, 336–358.
- POPINET, S. 2018 Numerical models of surface tension. *Annu. Rev. Fluid Mech.* **50**, 49–75.
- PREZIOSI, L., CHEN, K. & JOSEPH, D.D. 1989 Lubricated pipelining: stability of core-annular flow. *J. Fluid Mech.* **201**, 323–356.
- REDDY, S.C. & HENNINGSON, D.S. 1993 Energy growth in viscous channel flow. *J. Fluid Mech.* **252**, 209–238.
- RENARDY, Y. 1987 The thin-layer effect and interfacial stability in a two-layer Couette flow with similar liquids. *Phys. Fluids* **30** (6), 1627–1637.
- SCHMID, P.J. & HENNINGSON, D.S. 1994 Optimal energy density growth in Hagen-Poiseuille flow. *J. Fluid Mech.* **277**, 197–225.
- SHKADOV, V.YA. & SISOEVA, G.M. 1996 Instability of a two-layer capillary jet. *Intl J. Multiphase Flow* **22** (2), 363–377.

- SÖDERBERG, L.D. 2003 Absolute and convective instability of a relaxational plane liquid jet. *J. Fluid Mech.* **493**, 89–119.
- SÖDERBERG, L.D. & ALFREDSSON, P.H. 1998 Experimental and theoretical investigations of plane liquid jets. *Eur. J. Mech. B/Fluids* **17** (5), 689–737.
- SOUTH, M.J. & HOOPER, A.P. 1999 Linear growth in two-fluid plane Poiseuille flow. *J. Fluid Mech.* **381**, 121–139.
- TREFETHEN, L.N., TREFETHEN, A.E., REDDY, S.C. & DRISCOLL, T.A. 1993 Hydrodynamic stability without eigenvalues. *Science* **261** (5121), 578–584.
- VAN NOORDEN, T.L., BOOMKAMP, P.A.M., KNAAP, M.C. & VERHEGGEN, T.M.M. 1998 Transient growth in parallel two-phase flow: analogies and differences with single-phase flow. *Phys. Fluids* **10** (8), 2099–2101.
- YECKO, P. & ZALESKI, S. 2005 Transient growth in two-phase mixing layers. *J. Fluid Mech.* **528**, 43–52.
- YECKO, P., ZALESKI, S. & FULLANA, J.M. 2002 Viscous modes in two-phase mixing layers. *Phys. Fluids* **14** (12), 4115–4122.
- YIH, C.S. 1967 Instability due to viscosity stratification. *J. Fluid Mech.* **27** (2), 337–352.